Unsteady Adjoint Approach for Design Optimization of Flapping Airfoils

Byung Joon Lee[*] and Meng-Sing Liou[†]
NASA Glenn Research Center, Cleveland, OH, 44135, USA

This paper describes the work for optimizing the propulsive efficiency of flapping airfoils, i.e., improving the thrust under constraining aerodynamic work during the flapping flights by changing their shape and trajectory of motion with the unsteady discrete adjoint approach. For unsteady problems, it is essential to properly resolving time scales of motion under consideration and it must be compatible with the objective sought after. We include both the instantaneous and time-averaged (periodic) formulations in this study. For the design optimization with shape parameters or motion parameters, the time-averaged objective function is found to be more useful, while the instantaneous one is more suitable for flow control. The instantaneous objective function is operationally straightforward. On the other hand, the time-averaged objective function requires additional steps in the adjoint approach; the unsteady discrete adjoint equations for a periodic flow must be reformulated and the corresponding system of equations solved iteratively. We compare the design results from shape and trajectory optimizations and investigate the physical relevance of design variables to the flapping motion at on- and off-design conditions.

---

[*] NPP (NASA Post-doc. Program) Fellow, AIAA Member.
[†] Senior Technologist, Aeropropulsion Division, AIAA Associate Fellow.

Nomenclature

C_t = Time-averaged thrust coefficient

C_W = Power coefficient for time averaged work required to maintain the flapping motion

c = Chord length of airfoil

F, f = Objective functions for the sensitivity analysis and optimization

fr_h = Physical plunging frequency ($=U_\infty/\pi c$)

$h(t)$ = Time dependent equation of plunging motion

h_0 = Non-dimensional maximum amplitude of plunging motion

k = Reduced frequency ($= \pi fr_h c/U_\infty$)

kh = Nondimensional maximum body speed ($=kh_0$)

m = Index of frequency mode for superposed Fourier function

Re = Reynolds number

St = Strouhal number ($=2fr_h h_0 c/ U_\infty=2kh_0/\pi$)

T = Period of flapping motion

U_∞ = Flight (free stream) velocity

α = Angle of attack

β_p = Amplitudes of superposed Fourier functions

η = Propulsive efficiency ($=C_t U_\infty/ C_W$)

Ψ = Phase angle

$\mathbf{D}$ = General form of design variable vector

$\mathbf{Q}$ = Three-element vector of primitive variables $(p, u, v)^\mathrm{T}$.

$\mathbf{R}$ = Vector of discrete residual equations for incompressible Navier-Stokes equations

$\mathbf{R_s}$ = Vector of discrete residual equations for Steady-State fluxes

$\mathbf{R_t}$ = Vector of discrete unsteady time-derivative terms

$\mathbf{X}$ = Vector representing geometric variables of mesh

I.   Introduction

Development of efficient and accurate optimization approaches for aerospace applications is a focused interest under NASA's current Subsonic Fixed Wing Project. A special challenging topic in optimization is parameterization in both spatial and temporal dimensions, because they directly determine the details of physics to be captured and the scales in both dimensions affecting the design outcome. Hence, the design of micro-air-vehicles (MAV), whose flapping mechanisms are inspired primarily by flying animals, not only is of considerable current interest technologically, but also is a unique benchmark problem for developing optimization methodologies.

The interest in MAVs has become conspicuous since the 1990s [1–5]. The kinematics, dynamics, and flow characteristics of flapping wings have been investigated by experimental and computational means. Most studies have been devoted to understanding the mechanisms for lift, thrust and propulsive power, but only a few studies were concerned with optimization of the shape of flapping wing and the trajectory of motion. Lee et al. [5] designed a tadpole type of flapping airfoil in their parametric study based on computational fluid dynamics (CFD) analysis. Tuncer and Kaya [6, 7] designed a bi-plane configuration by including parameters of sinusoidal motion to maximize propulsive efficiency using a gradient-based approach. Most previous design works were conducted focusing on uniform sinusoidal plunging and pitching motions, where the number of design parameters is small (limited to two or three), because of a prohibitive computational cost in unsteady optimization problems—even with an efficient gradient-based method. In a realistic aerodynamic shape optimization, the number of design

parameters needed to adequately describe an airfoil shape in transonic flow can vary from O(10) to O(100), even for a two-dimensional airfoil application [8–10]. As a result, the design cost of optimization based on CFD is expensive, even with today's computation power; hence a judicious choice of optimization approach for the current problem is warranted. In our study, we adopt the approach of using adjoint sensitivity analyses [8–10] in our aerodynamic shape and trajectory optimizations for flapping airfoils.

The situation in the trajectory optimization becomes more acute if one intends to explore an extended design space by using more non-harmonic trajectory functions. It is known that the flapping motion results in a strong nonlinear wake flow where propulsive thrust is generated [11, 12]. Vytla et al. found a bifurcation behavior of vortex shedding which depends on the initial attitude of the airfoil [13]. In addition, they found that the bifurcation pattern can result from a disturbance during the flapping motion and the flapping creatures can change the flow pattern around their wing from one mode to a favorable one by making use of disturbances in motion. In other words, if the design parameters for the flapping motion include more disturbances of various modes, the optimal motion can be more efficient. To realize this possibility in the present work, the motion trajectory will be represented by considering a large number of different modes.

The adjoint approach has been regarded as a very efficient sensitivity analysis method for aerodynamic shape optimization because the computational time cost is almost independent of the number of design variables [8–10]. To apply this method to an unsteady aerodynamic application, two different ways of accounting for physical time can be taken. One treats it in an instantaneous manner (a local approach) for dealing with phenomena in small time scale, e.g., for flow control. In this case, it is possible to extend the steady-state adjoint formulation in a straightforward fashion by adding a source-like term from the physical time difference. Kim et al.

[8] applied this approach for the design of a high-lift device at high angles of attack, where a large flow separation is observed during the design optimization. The other approach treats the unsteady optimization problem in a time-averaged manner (a global approach), and it is used in this study for optimization of shape and trajectory. In order to differentiate the time-integrated objective function, the same number of adjoint vectors and adjoint equations as that of physical time steps should be prepared. Nadarajah and Jameson proposed a reverse time-integration method with a terminal condition to evaluate the sensitivities of the time-averaged objective function for two-dimensional unsteady compressible flow [14]. Their formulation, however, is valid only when the time integration is conducted from initial to final physical time step. Thus, the solution of the flow problem has to be stored for all time levels over which the optimization is solved. In the case of three-dimensional problems or two-dimensional problems that are very sensitive to time steps, the storage of flow properties can be prohibitively large. Yamaleev et al. [15, 16] devised a local-in-time, time-dependent adjoint method to reduce the memory size by dividing the whole time domain into sub-intervals for several two-dimensional unsteady design problems. They reformulated the sub-interval form by obtaining the terminal adjoint vector from previous design iteration to have a closed system equation. Their approach provides reasonable accuracy for the sensitivities, showing similar optimal solution to Nadarajah's formulation. However, the assumption is not mathematically rigorous and may affect the accuracy of the sensitivity in case that flow pattern changes remarkably between the design iterations. Instead of assuming the terminal conditions, especially for periodic unsteady flows, we suggest to adopt periodic conditions of flow derivatives and adjoint vectors and to solve the sub-interval adjoint system equations by an iterative manner.

In the present work, we develop an unsteady discrete adjoint code that aims to provide accurate sensitivities for a periodic problem such as flapping motions in a time-averaged manner. Based on this strategy, we perform the design for optimal shape and motion of a flapping airfoil. Finally efforts are made to identity parameters that are effective for increasing flapping performance at on- and off-design conditions.

II.   Sensitivity Analysis for Unsteady Flows

A. Unsteady Discrete Adjoint Equations Formulated in Instantaneous Manner

As mentioned above, an instantaneous adjoint formulation can be useful for optimal flow control problems by revealing the flow physics responsible for aerodynamic performances. In these problems, the objective function is defined as a function of flow variables at each time step, as in the steady-state formulation. As a result, the formulation remains essentially the same except that the treatment of the time derivative is included as a source-like term. The source term results from the physical time derivative, which in our case is approximated by a three-point backward Euler implicit method. As the flapping airfoil under study is moving at low speed, the resulting flow phenomena will be described with incompressible Navier-Stokes equations. The system of equations is rendered hyperbolic by incorporating the pseudo-compressibility concept [17]. The final discretized equations written in delta form between two consecutive iterations in a pseudo-time formulation with step $\Delta\tau$ become

$$\left[\frac{\mathbf{I}}{J\Delta t}+\left(\frac{\partial\mathbf{R_s}}{\partial\mathbf{Q}}+\frac{\partial\mathbf{R_t}}{\partial\mathbf{Q}}\right)^m_{n+1}\right]\Delta\mathbf{Q}^{m+1}_{n+1}=-\left\{\mathbf{R_s}+\mathbf{R_t}\right\}^m_{n+1}=-\mathbf{R}^m_{n+1},$$

$$\mathbf{R}_{\mathbf{t}n+1}=\frac{1.5\mathbf{Q}_{n+1}-2\mathbf{Q}_n+0.5\mathbf{Q}_{n-1}}{J\Delta t}$$

(1)

where J is the Jacobian matrix of transformation between the Cartesian and body-fitted coordinates, τ and superscript m refer to pseudo time, and t and n to physical time. $\mathbf{R_s}$ and $\mathbf{R_t}$ are the discretized forms of the spatial-derivative and time-derivative terms in the Navier-Stokes equations, respectively. The discrete residual $\mathbf{R}$ of the unsteady flow equations is the sum of these two discrete derivatives, and the time-accurate solution is obtained when $\mathbf{R} = 0$. For the design problem, the residual is a function of flow solution $\mathbf{Q}$, grid position $\mathbf{X}$, and design variables $\mathbf{D}$. Hence,

$$\mathbf{R} = \mathbf{R}_s + \mathbf{R}_t = \mathbf{R}\{\mathbf{Q}, \mathbf{X}, \mathbf{D}\} = 0 \tag{2}$$

Similarly, the aerodynamic objective function f is also dependent on $\mathbf{Q}$, $\mathbf{X}$, and $\mathbf{D}$,

$$f = f(\mathbf{Q}, \mathbf{X}, \mathbf{D}) \tag{3}$$

Sensitivity derivatives of the aerodynamic functions with respect to design variables $\mathbf{D}$ are calculated by differentiating Eqs. (2) and (3):

$$\frac{d\mathbf{R}}{d\mathbf{D}} = \frac{\partial \mathbf{R}}{\partial \mathbf{Q}} \frac{d\mathbf{Q}}{d\mathbf{D}} + \frac{\partial \mathbf{R}}{\partial \mathbf{X}} \frac{d\mathbf{X}}{d\mathbf{D}} + \frac{\partial \mathbf{R}}{\partial \mathbf{D}} = 0 \tag{4}$$

$$\frac{df}{d\mathbf{D}} = \frac{\partial f}{\partial \mathbf{Q}} \frac{d\mathbf{Q}}{d\mathbf{D}} + \frac{\partial f}{\partial \mathbf{X}} \frac{d\mathbf{X}}{d\mathbf{D}} + \frac{\partial f}{\partial \mathbf{D}} \tag{5}$$

where the design variables vector, $\mathbf{D}$, is in general time-dependent and affects the flow property at the corresponding physical time step. The quantities $\mathbf{Q}_{n-1}$ and $\mathbf{Q}_n$ are known and regarded as fixed with respect to the design parameters. Hence, we shall denote $\mathbf{Q}_{n+1}$ by $\mathbf{Q}$ hereafter for simplicity. In the adjoint method, the sensitivity derivatives of the aerodynamic functions are obtained by combining Eqs. (4) and (5) through the introduction of the Lagrangian multiplier matrix Λ:

$$\frac{df}{d\mathbf{D}} = \frac{\partial f}{\partial \mathbf{Q}} \frac{d\mathbf{Q}}{d\mathbf{D}} + \frac{\partial f}{\partial \mathbf{X}} \frac{d\mathbf{X}}{d\mathbf{D}} + \frac{\partial f}{\partial \mathbf{D}} + \mathbf{\Lambda}^T \left(\frac{\partial \mathbf{R}}{\partial \mathbf{Q}} \frac{d\mathbf{Q}}{d\mathbf{D}} + \frac{\partial \mathbf{R}}{\partial \mathbf{X}} \frac{d\mathbf{X}}{d\mathbf{D}} + \frac{\partial \mathbf{R}}{\partial \mathbf{D}} \right) \tag{6}$$

where $\mathbf{\Lambda}$ is a three-element adjoint vector consisting of the Lagrangian multipliers $(\lambda_1, \lambda_2, \lambda_3)^T$ corresponding to the primitive variables $(p, u, v)^T$. The geometrical sensitivity vector $d\mathbf{X}/d\mathbf{D}$ can be obtained by differentiating the grid generation code. In the present work, finite difference approximation is applied for simplicity. Rearranging Eq. (6) to factor out $d\mathbf{Q}/d\mathbf{D}$ yields the following equation:

$$\frac{df}{d\mathbf{D}} = \frac{\partial f}{\partial \mathbf{X}} \frac{d\mathbf{X}}{d\mathbf{D}} + \frac{\partial f}{\partial \mathbf{D}} + \mathbf{\Lambda}^T \left(\frac{\partial \mathbf{R}}{\partial \mathbf{X}} \frac{d\mathbf{X}}{d\mathbf{D}} + \frac{\partial \mathbf{R}}{\partial \mathbf{D}} \right) + \left(\frac{\partial f}{\partial \mathbf{Q}} + \mathbf{\Lambda}^T \frac{\partial \mathbf{R}}{\partial \mathbf{Q}} \right) \frac{d\mathbf{Q}}{d\mathbf{D}} \tag{7}$$

By excluding the computationally intensive term $d\mathbf{Q}/d\mathbf{D}$, the sensitivity derivatives of the aerodynamic functions can be considerably reduced to

$$\frac{df}{d\mathbf{D}} = \frac{\partial f}{\partial \mathbf{X}}\frac{d\mathbf{X}}{d\mathbf{D}} + \frac{\partial f}{\partial \mathbf{D}} + \mathbf{\Lambda}^T\left(\frac{\partial \mathbf{R}}{\partial \mathbf{X}}\frac{d\mathbf{X}}{d\mathbf{D}} + \frac{\partial \mathbf{R}}{\partial \mathbf{D}}\right) \tag{8}$$

This is possible if and only if the coefficient of $d\mathbf{Q}/d\mathbf{D}$ vanishes for a proper vector $\mathbf{\Lambda}$. After including the derivatives of $\mathbf{R_t}$ with respect to $\mathbf{Q}$, this becomes

$$\frac{\partial \mathbf{R}}{\partial \mathbf{Q}}^T \mathbf{\Lambda} + \frac{\partial f}{\partial \mathbf{Q}} = \left(\frac{\partial \mathbf{R_s}}{\partial \mathbf{Q}}^T + \frac{1.5\mathbf{I}}{J\Delta t}\right)\mathbf{\Lambda} + \frac{\partial f}{\partial \mathbf{Q}} = \mathbf{0} \tag{9}$$

An iterative procedure will be required to obtain the solution vector $\mathbf{\Lambda}$ in Eq. (9), as its coefficient matrix can be of a large dimension. Mimicking the solution procedure for solving the flow variables in Eq. (1), the backward Euler implicit method with pseudo-time marching is also used here. Hence,

$$\left(\frac{\mathbf{I}}{J\Delta\tau} + \frac{\partial \mathbf{R_s}}{\partial \mathbf{Q}}^T + \frac{1.5\mathbf{I}}{J\Delta t}\right)\Delta\mathbf{\Lambda}^{m+1} = -\left(\frac{\partial \mathbf{R_s}}{\partial \mathbf{Q}}^T + \frac{1.5\mathbf{I}}{J\Delta t}\right)\mathbf{\Lambda}^m - \frac{\partial f}{\partial \mathbf{Q}} \tag{10}$$

$$\mathbf{\Lambda}^{m+1} = \mathbf{\Lambda}^m + \Delta\mathbf{\Lambda}^{m+1}$$

Note that for steady-state computations, the physical time term vanishes by setting the physical time step Δt to infinity. Boundary conditions in the adjoint variable methods are also derived similarly as in Eq. (9):

$$\left(\frac{\partial \mathbf{R_s}}{\partial \mathbf{Q}}^T + \frac{1.5\mathbf{I}}{J\Delta t}\right)\mathbf{\Lambda} + \frac{\partial \mathbf{R}_{sB}}{\partial \mathbf{Q}}^T \mathbf{\Lambda}_B + \frac{\partial f}{\partial \mathbf{Q}} = \mathbf{0} \tag{11a}$$

and

$$\frac{\partial \mathbf{R_s}}{\partial \mathbf{Q}_B}^T \mathbf{\Lambda} + \left(\frac{\partial \mathbf{R}_{sB}}{\partial \mathbf{Q}_B}^T + \frac{1.5\mathbf{I}}{J\Delta t}\right)\mathbf{\Lambda}_B + \frac{\partial f}{\partial \mathbf{Q}_B} = \mathbf{0} \tag{11b}$$

where subscript B denotes the boundary cells.

B. Unsteady Discrete Adjoint Equations Formulated in Time-Averaged Manner

The time-averaged formulation is useful for shape optimization where the mean performance is important. In this case, the objective function over a period can be expressed in a discrete time-integration form as

$$F = \sum_{n=N_m+1}^{N_{m+1}} f_n(\mathbf{Q}(t^n), \mathbf{X}(t^n), \mathbf{D}) \tag{12}$$

where t^n is the nth physical time step within the $(m+1)^{th}$ period. N_m and N_{m+1} denote the final time steps of the mth and $(m+1)^{th}$ periods, respectively. f_n is the considered function at t^n (the nth time step) in the time averaged form for a time span of interest (T), divided by (N_{m+1}- N_m) time increments $\Delta t/T$. For example, for minimizing the drag coefficient, we take $f_n = C_d(t_n) \, \Delta t \, /T$. Hereafter, $\mathbf{Q}(t^n)$ and $\mathbf{X}(t^n)$ are simply denoted by $\mathbf{Q}_n$ and $\mathbf{X}_n$, respectively. The sensitivity of the cost function F can be represented as

$$\frac{dF}{d\mathbf{D}} = \sum_{n=N_m+1}^{N_{m+1}} \left\{ \frac{\partial f_n(\mathbf{Q}_n, \mathbf{X}_n, \mathbf{D})}{\partial \mathbf{Q}_n} \frac{d\mathbf{Q}_n}{d\mathbf{D}} + \frac{\partial f_n(\mathbf{Q}_n, \mathbf{X}_n, \mathbf{D})}{\partial \mathbf{X}_n} \frac{d\mathbf{X}_n}{d\mathbf{D}} + \frac{\partial f_n(\mathbf{Q}_n, \mathbf{X}_n, \mathbf{D})}{\partial \mathbf{D}} \right\}. \tag{13}$$

Different from the expression in the previous section, there are many flow derivative terms, $\{d\mathbf{Q}_n/d\mathbf{D}\}$, which are destined to be excluded in order to reduce the computation cost associated with these terms. Thus, these terms should be eliminated as before by combining adjoint vectors and residual equations. The residual equation at the nth time step with second-order time accuracy can be represented as

$$\begin{aligned}\mathbf{R}_n &= \mathbf{R}_n\left(\mathbf{Q}_n, \mathbf{Q}_{n-1}, \mathbf{Q}_{n-2}, \mathbf{X}_n, \mathbf{D}\right) \\ &= \mathbf{R}_{s,n}\left(\mathbf{Q}_n, \mathbf{X}_n, \mathbf{D}\right) + \frac{1.5\mathbf{Q}_n - 2\mathbf{Q}_{n-1} + 0.5\mathbf{Q}_{n-2}}{J\Delta t} = 0\end{aligned} \tag{14}$$

Thus

$$\frac{\partial \mathbf{R}_{s,n}}{\partial \mathbf{Q}_n} \frac{d\mathbf{Q}_n}{d\mathbf{D}} + \frac{\partial \mathbf{R}_{s,n}}{\partial \mathbf{X}_n} \frac{d\mathbf{X}_n}{d\mathbf{D}} + \frac{3}{2J\Delta t} \frac{d\mathbf{Q}_n}{d\mathbf{D}} - \frac{2}{J\Delta t} \frac{d\mathbf{Q}_{n-1}}{d\mathbf{D}} + \frac{1}{2J\Delta t} \frac{d\mathbf{Q}_{n-2}}{d\mathbf{D}} + \frac{\partial \mathbf{R}_{s,n}}{\partial \mathbf{D}} = 0 \tag{15}$$

The sensitivity equation, after combining with the residual equations at every physical time step, becomes

$$
\begin{aligned}
\frac{dF}{d\mathbf{D}} = \sum_{n=N_m+3}^{N_{m+1}} & \left[\frac{\partial f_n}{\partial \mathbf{Q}_n}\frac{d\mathbf{Q}_n}{d\mathbf{D}} + \frac{\partial f_n}{\partial \mathbf{X}_n}\frac{d\mathbf{X}_n}{d\mathbf{D}} + \frac{\partial f_n}{\partial \mathbf{D}} + \boldsymbol{\Lambda}_n^{T} \left[\begin{array}{l} \dfrac{\partial \mathbf{R}_{s,n}}{\partial \mathbf{Q}_n}\dfrac{d\mathbf{Q}_n}{d\mathbf{D}} + \dfrac{\partial \mathbf{R}_{s,n}}{\partial \mathbf{X}_n}\dfrac{d\mathbf{X}_n}{d\mathbf{D}} + \dfrac{3}{2J\Delta t}\dfrac{d\mathbf{Q}_n}{d\mathbf{D}} \\[8pt] -\dfrac{2}{J\Delta t}\dfrac{d\mathbf{Q}_{n-1}}{d\mathbf{D}} + \dfrac{1}{2J\Delta t}\dfrac{d\mathbf{Q}_{n-2}}{d\mathbf{D}} + \dfrac{\partial \mathbf{R}_{s,n}}{\partial \mathbf{D}} \end{array} \right] \right] \\[12pt]
+ & \frac{\partial f_{N_m+2}}{\partial \mathbf{Q}_{N_m+2}}\frac{d\mathbf{Q}_{N_m+2}}{d\mathbf{D}} + \frac{\partial f_{N_m+2}}{\partial \mathbf{X}_{N_m+2}}\frac{d\mathbf{X}_{N_m+2}}{d\mathbf{D}} + \frac{\partial f_{N_m+2}}{\partial \mathbf{D}} + \boldsymbol{\Lambda}_{N_m+2}^{T} \left[\begin{array}{l} \dfrac{\partial \mathbf{R}_{s,N_m+2}}{\partial \mathbf{Q}_{N_m+2}}\dfrac{d\mathbf{Q}_{N_m+2}}{d\mathbf{D}} + \dfrac{\partial \mathbf{R}_{s,N_m+2}}{\partial \mathbf{X}_{N_m+2}}\dfrac{d\mathbf{X}_{N_m+2}}{d\mathbf{D}} + \dfrac{3}{2J\Delta t}\dfrac{d\mathbf{Q}_{N_m+2}}{d\mathbf{D}} \\[8pt] -\dfrac{2}{J\Delta t}\dfrac{d\mathbf{Q}_{N_m+1}}{d\mathbf{D}} + \dfrac{1}{2J\Delta t}\dfrac{d\mathbf{Q}_{N_m}}{d\mathbf{D}} + \dfrac{\partial \mathbf{R}_{S,N_m+2}}{\partial \mathbf{D}} \end{array} \right] \\[12pt]
+ & \frac{\partial f_{N_m+1}}{\partial \mathbf{Q}_{N_m+1}}\frac{d\mathbf{Q}_{N_m+1}}{d\mathbf{D}} + \frac{\partial f_{N_m+1}}{\partial \mathbf{X}_{N_m+1}}\frac{d\mathbf{X}_{N_m+1}}{d\mathbf{D}} + \frac{\partial f_{N_m+1}}{\partial \mathbf{D}} + \boldsymbol{\Lambda}_{N_m+1}^{T} \left[\begin{array}{l} \dfrac{\partial \mathbf{R}_{s,N_m+1}}{\partial \mathbf{Q}_{N_m+1}}\dfrac{d\mathbf{Q}_{N_m+1}}{d\mathbf{D}} + \dfrac{\partial \mathbf{R}_{s,N_m+1}}{\partial \mathbf{X}_{N_m+1}}\dfrac{d\mathbf{X}_{N_m+1}}{d\mathbf{D}} + \dfrac{3}{2J\Delta t}\dfrac{d\mathbf{Q}_{N_m+1}}{d\mathbf{D}} \\[8pt] -\dfrac{2}{J\Delta t}\dfrac{d\mathbf{Q}_{N_m}}{d\mathbf{D}} + \dfrac{1}{2J\Delta t}\dfrac{d\mathbf{Q}_{N_m-1}}{d\mathbf{D}} + \dfrac{\partial \mathbf{R}_{s,N_m+1}}{\partial \mathbf{D}} \end{array} \right]
\end{aligned}
\tag{16}
$$

If the flapping motion is completely periodic, then we can use the following identities:

$$
\frac{d\mathbf{Q}_{N_m}}{\partial \mathbf{D}} = \frac{d\mathbf{Q}_{N_{m+1}}}{\partial \mathbf{D}} \quad , \quad \frac{d\mathbf{Q}_{N_m-1}}{\partial \mathbf{D}} = \frac{d\mathbf{Q}_{N_{m+1}-1}}{\partial \mathbf{D}}
\tag{17}
$$

As before, we obtain the adjoint equations for every physical time step by eliminating the coefficients associated with the flow derivatives term $\{d\mathbf{Q}_n/d\mathbf{D}\}$:

$$
\frac{\partial f_n}{\partial \mathbf{Q}_n} + \boldsymbol{\Lambda}_n^{T}\frac{\partial \mathbf{R}_{s,n}}{\partial \mathbf{Q}_n} + \frac{3\boldsymbol{\Lambda}_n}{2J\Delta t} - \frac{2\boldsymbol{\Lambda}_{n+1}}{J\Delta t} + \frac{\boldsymbol{\Lambda}_{n+2}}{2J\Delta t} = \mathbf{0}, \quad (N_m+1 \le n \le N_{m+1})
$$

$$
\text{Periodic Conditions: } \boldsymbol{\Lambda}_{N_{m+1}+1} = \boldsymbol{\Lambda}_{N_m+1}, \ \boldsymbol{\Lambda}_{N_{m+1}+2} = \boldsymbol{\Lambda}_{N_m+2}
\tag{18}
$$

The adjoint system equations are solved in a reverse time order by beginning with the equation at the $(N_{m+1})^{th}$ physical time and ending at $(N_m+1)^{th}$ time. Hence, this process is called the reverse time integration, as it traces from the later to earlier physical time steps. If the adjoint equations are all satisfied with the correct $\boldsymbol{\Lambda}_n$, then the sensitivity will be integrated by

$$
\frac{dF}{d\mathbf{D}} = \sum_{n=1}^{N} \left[\frac{\partial f_n}{\partial \mathbf{X}_n}\frac{d\mathbf{X}_n}{d\mathbf{D}} + \frac{\partial f_n}{\partial \mathbf{D}} + \boldsymbol{\Lambda}_n^{T} \left[\frac{\partial \mathbf{R}_{s,n}}{\partial \mathbf{X}_n}\frac{d\mathbf{X}_n}{d\mathbf{D}} + \frac{\partial \mathbf{R}_{s,n}}{\partial \mathbf{D}} \right] \right]
\tag{19}
$$

However, the initial adjoint vectors needed to begin the time integration, $\mathbf{\Lambda}_{Nm+1+1}$ and $\mathbf{\Lambda}_{Nm+1+2}$, are yet to be determined. It is assumed that the initial guess on their values is immaterial and can be arbitrary, since they will be iteratively updated until convergence is declared. Thus, we set the initial values of $\mathbf{\Lambda}_{Nm+1+1}$ and $\mathbf{\Lambda}_{Nm+1+2}$ to be zero and update by the periodic condition in Eq. (18) as the iteration goes over. The gradient can be determined if the following criterion is satisfied by measuring some error E between the qth and $(q+1)^{th}$ steps,

$$E(q+1) = \left\| \mathbf{G}^{q+1} - \mathbf{G}^q \right\| / N_{DV} \leq \varepsilon \tag{20}$$

where $\mathbf{G}^q$ is the sensitivity vector at q^{th} iteration, N_{DV} is the number of design variables, and ε is a tolerance for convergence. The boundary conditions are handled in the same manner as for the instantaneous formulation.

III.   Design Formulation

A. Design Parameters

Although a non-harmonic rigid body motion is the focus of this study, we shall use the uniform sinusoidal motion for plunging for validation because of availability of experimental data and other computational reports. The equation for a baseline rigid body motion is defined as follows:

$$\text{Baseline plunge motion: } h = h_0 \cos(2\pi fr_h t) \tag{21}$$

$$\text{Plunge frequency: } fr_h = U_\infty k / \pi c \tag{22}$$

where h_0 is the reduced plunge amplitude, k is the reduced frequency, and c is the chord length of airfoil. Here, several modes of sinusoidal functions with sought-after amplitudes and periods, as given in Eq. (23), are superimposed to the baseline plunge motion to achieve optimization. The general flapping motion is now represented by m additional harmonics that are compatible with the period of the baseline motion.

$$h_p(t) = h_0 \cdot \begin{cases} \beta_p \sin(2m\pi fr_h t) & \text{if } p = 2m-1 \\ \beta_p \cos(2m\pi fr_h t) & \text{if } p = 2m \end{cases}, \quad m=1, 2, \ldots, 5 \tag{23}$$

The total number of design parameters is 10 in the trajectory study: they are 10 amplitudes, β_p. The constraints for β_p are limited between -1.0 and 1.0, except β_2 whose frequency is the same as the baseline. Thus, we set $0 \leq \beta_2 \leq 2$ so that the motion equation can represent non-flapping flow as well. Now the complete motion is expressed as follows:

$$h(t) = h_0 \left\{ \cos(2\pi fr_h t) + \sum_{m=1}^{5} \left\{ \beta_{2m-1} \sin(2m\pi \cdot fr_h t) + \beta_{2m} \cos(2m\pi \cdot fr_h t) \right\} \right\} \tag{24}$$

In addition to the parameters controlling the flapping motion, the geometry of an airfoil is also responsible for producing thrust and lift forces, just as thin and thick airfoils will induce different

amounts of vortex shedding. Thus, optimization for the shape of airfoil is also conducted to investigate its effectiveness in comparison to the flapping motion alone. The Hicks-Henne functions [18], as shown in Fig. 1, are adopted to describe the airfoil shape. Here 10 functions with different peak positions are used on the upper and lower surfaces, resulting in 20 design variables in total. The amplitudes of all functions, contributing to the deformation of the airfoil, are constrained by the limit from $-0.006c$ to $0.006c$.

B. Cost Functions

For the flapping motion, thrust, lift, and power coefficients are regarded as major performance factors. To give an overall performance through the entire unsteady motion, these coefficients are evaluated in a time-averaged manner. The thrust coefficient is based on the integration of the negative drag coefficient over a flapping period as follows:

$$C_t = \frac{1}{T}\int_t^{t+T}\{-C_d(t)\}dt \tag{25}$$

Here, T is the period of the motion and $C_d(t)$ represents the time-varied drag coefficient. The power coefficient C_W is a time-averaged work required to maintain the flapping motion.

$$C_W = \frac{1}{T}\int_t^{t+T}\int_A C_p(\mathbf{V}\cdot d\mathbf{A})dt \tag{26}$$

Here, it is assumed that the mass and inertia of the airfoil are negligible. A denotes the control surface of the geometry, $\mathbf{V}$ is the airfoil velocity, and C_p is the pressure coefficient at a surface element with the area vector $d\mathbf{A}$. The propulsive efficiency η is defined as the ratio of the thrusting power to the power coefficient:

$$\eta = \frac{C_t U_\infty}{C_W} \tag{27}$$

where U_∞ is the free-stream velocity or the velocity of the flapping airfoil in still air. The time-averaged lift coefficient is evaluated in a similar manner:

$$C_l = \frac{1}{T} \int_t^{t+T} C_l(t)dt \qquad (28)$$

Depending upon the objective of an optimization problem, any one of the above performance indicators or a combination of them may be chosen. For a hovering motion, the lift coefficient and power coefficient can be considered as the objective and constraint, respectively. In the study presented here, the propulsive efficiency is to be maximized so that the rate of increase in thrust is faster than that of power input during the optimization.

IV.   Validation of Flow Analysis and Sensitivity Analysis

A. Validation of Force Prediction

The solver adopted for the current study is validated through predictions of time-varying aerodynamic coefficients on NACA 0012 airfoil for two drag inducing conditions where the Strouhal number is small and the Reynolds number moderate. It is reported that the contribution of viscous drag reaches about 70% of total drag [24] and the time-accuracy of the force measurement is highly sensitive to the grid distributions in these conditions. The flow is assumed laminar as the effects of Reynolds number did not appear significant for MAV flapping wings in previous work [1–7, 11–13, 20, 21]. We specify the flapping motion by imposing the velocity and displacement at grid points on the airfoil according to Eq. (24). Since there is no experimental data provided, we compared the current force measurement with the previously reported CFD results by Young [23] and Lian et al. [24] The first case is at the reduced frequency, k, of 3.93, non-dimensional plunging amplitude, h_0, of 0.0125 so that the resulted Strouhal number, St, is 0.03. Figure 2 presents the results of C_d and C_l from three different densities of C-type grid: coarse (257x49), intermediate (513x49), and fine (1025x193) and a fine (513x173) O-type grid. Besides the coarse C-type grid where the number of grid points along the airfoil direction is not enough to provide an accurate prediction of drag force, solutions of all other grids fall between those reported in [24]. The lift coefficients of all grids, including coarse grid, show high coincidence with each other. Figure 3 shows the histories of drag and lift forces at the same reduced frequency but with a doubled plunging amplitude (hence doubling St) of h_0=0.025, and Strouhal number, St, of 0.06. In this condition, the discrepancy between coarse grid and other grids is considerably reduced from the previous case. Thus, it can be reasoned that the effect of viscous force gets less dominant and the grid dependency gets weaker as the

Strouhal number increases. Since the purpose of current study is to perform design optimization for propulsive efficiency, the force prediction is validated over a wide range of conditions covering the most-studied flapping flight regimes. The efficiency curve with respect to kh (non-dimensional flapping velocity) in Figure 4 confirms the force prediction of current study is well validated. Here, the non-dimensional body speed is usually calculated by a multiplication of reduced frequency and wake width, which is the excursion distance of the trailing edge. For the pure plunging motion, the plunging amplitude is regarded as the excursion distance. The reduced frequency is usually calculated by $2\pi f r_h c/U_\infty$. However, in the present work it is defined as $\pi f r_h c/U_\infty$, in order to be consistent with that used in the experimental and other CFD results [13, 20, 21]. Thus, the kh value in the present work is half of that in Ref. [23]. We compare the force predictions on three C-type grids with different sizes, 513x49, 513x97 and 1025x193, with experimental data [11] and Young's CFD computation [23] at the range of kh from 0 to 0.6 (0~1.2 in [11, 23]) at the Reynolds number of 20,000. The plunging amplitude is fixed at 0.175 and reduced frequency is varying from 0 to 3.4. Similarly to results in previous reports, the peak of efficiency is obtained around kh=0.1875 (0.375 in [11, 23]). In the following Section V, an optimization case of symmetric airfoil will be presented at this highest efficiency point.

B. Validation of Flow Analysis for Wake Profiles

In order to study the design of a more practical case of lifting airfoil, the asymmetric SD7003 airfoil [19] was used in our simulations, while previous experimental works [13, 20, 21] were used as basis for comparison. The Reynolds number for all validation cases of plunging motion is 10,000. The reduced frequency, k, is 3.93; the plunging amplitude, h_0, is 0.05; and the angle of attack is 4°. An O-type structured grid around the airfoil is used with three grid sizes of 243×126 (coarse), 243×265 (medium), and 486×358 (fine) for the convergence study. For validation of

the baseline flow solver, the CFD results are compared with experimental data for a pure plunge motion [19].

The computed vorticity contours at selected physical time steps for the plunge motion is presented in Fig. 5(a), in which the CFD results from the 20th cycle of the motion on the fine grid are used. The experimental contours, shown in Fig. 5(b), are the phase-averaged particle image velocimetry (PIV) data over 120 periods. It shows that the computed solutions at various phases are in good qualitative agreement with the experimental observation. The wake profiles at two chords away from the leading edge are compared in Figs. 6, for each of the four phases given in Figs. 6. In addition, the results of three grids are included, indicating that the flow patterns are essentially grid converged, except at $\Psi = 270°$, where the fine-grid solution departs from the other two solutions significantly; overall, even the coarse-grid solution appears to capture essential physics well. Hence, in the interest of reducing computation time, we chose to use the coarse grid for the optimization. Furthermore, the resolution of the physical time step is another factor that can affect the accuracy of an unsteady flow analysis. The time steps selected are 60, 100, 200, 500, and 1000 steps for a period, and the corresponding results are given in Fig. 7. The profile predicted by 200 physical time steps is nearly identical to that of 1000 physical time steps. However, the results of 100 and 60 steps show the structure of wake vortices as somewhat dissipated. Hence, 200 physical time steps in a period will be used in the design optimization.

C. Validation of Sensitivity Analysis for Steady and Unsteady Incompressible Viscous Flows

Next, we present the validation of the sensitivity analysis, based on the discrete adjoint approach, for steady as well as unsteady flows. For both cases, geometrical variables are taken as design variables. In order to validate the differentiation of the incompressible RANS solver, the

sensitivities from the adjoint solver are compared with finite-differenced gradients (referred to as FDM) for a steady flow over the SD7003 airfoil at the angle of attack of 5° and Reynolds number of 10,000. The objective function is the lift coefficient, and 20 Hicks-Henne functions are used as design variables (10 on the upper and 10 on the lower surfaces, respectively). As shown in Fig. 8, all the sensitivities by the adjoint solver are in very good agreement with the results by FDM with a step size of $O(10^{-7})$.

For the sensitivity analysis of unsteady flow, the same geometry is applied at an angle of attack of 4° as the initial posture, with a plunging amplitude of 0.05, reduced frequency of 3.93, and Reynolds number of 10,000. As mentioned above, in order to prevent possible violation of periodic assumption of current adjoint formulation during the flow and sensitivity analyses, only the plunge motion, the simplest flapping motion, is considered for the validation and design optimizations of the present work. It is reported that a nonlinear bifurcation in the wake flow can happen during some pitching or pitching combined with plunging motions at certain conditions [13]. The sensitivities from the time-averaged approach are compared with the FDM with the step size of $O(10^{-5})$ in Figs. 9–11. Recall that the motion and flow pattern are assumed periodic in the present adjoint formulation. Therefore, the time averaged coefficients at the 20th flapping cycle, at which the motion has attained periodic characteristics, is used for the validation and design optimization. Figure 9 is the sensitivities of lift coefficient with respect to the shape parameters. The design variables numbered from 1 to 10 denote the geometric changes from leading edge to trailing edge on the upper surface, and those of 11 to 20 refer to the geometric changes on the lower surface. It is shown that the sensitivities show a good comparison with the FDM (step size of $O(10^{-5})$) except in the upper leading edge regions where complicated vortex structures are observed. In other words, the region is still showing aperiodic characteristics, and

the assumption of periodic condition for the adjoint formulation is not satisfied locally. To investigate the effect of local aperiodic flow characteristics on the sensitivities, we present the history of thrust coefficient and its finite differenced sensitivities with respect to select design parameters during 20th cycles in figure 10. It can be observed that the FDM sensitivities are still varying considerably even between 19th and 20th cycles where the thrust coefficient already converges to a certain value with a very small, i.e., $O(10^{-5})$, amount of deviation. Among the design parameters, the leading edge parameters on the upper surface denoted by parameters 1, 2, 4 show larger variations while others, 5 and 8, which are relatively closer to the trailing edge region, have already converged. Thus, it can be reasoned that a small local aperiodic flow pattern (possibly due to both of the numerical or physical aperiodicity) affects the accuracy of the sensitivities, especially at the leading edge region. Overall, however, the direction of the gradient vector is almost same as those calculated by FDM. The convergence characteristics of the sensitivities of using different numbers of outer iterations are presented in Fig. 11. In the figure, the adjoint sensitivities of the thrust coefficient with respect to the shape parameters from each of outer iterations are compared with FDM. The first iteration with the initial conditions $\mathbf{\Lambda}_{Nm+1}=0$ and $\mathbf{\Lambda}_{Nm+2}=0$ clearly provides a poor accuracy. As the number of iterations increases, the sensitivities converge rapidly. After the 4th iteration, the accuracy of sensitivities appears nearly unchanged if $E \leq 0.01$. Hence, the criterion $E \leq 0.01$ is used throughout the study.

V.   Optimization and Performance at On- and Off-design Conditions

For the design of a flapping wing with plunging motions, two shape optimization cases and one trajectory optimization are considered to demonstrate the capability of the current design approach. The objective of all optimization cases is to maximize propulsive efficiency. Shape optimizations are carried out on symmetric and asymmetric airfoils, respectively, by using 20 Hicks-Henne functions. The constraints include bounds on the geometrical parameters to prevent too severe change in shape. For the trajectory optimization, non-harmonic motion is sought after by using the amplitudes of 10 superposed Fourier functions as design parameters. The frequency and amplitude of mean motion are not included in the set of design variables because those effects will be investigated for off-design conditions by varying kh, a representative non-dimensional body speed. The optimization algorithm used is the BFGS (Broyden-Fletcher-Goldfarb-Shanno) non-constrained line search method [22].

A. Shape Optimization for a Symmetric Airfoil (NACA 0012)

As a validation of shape optimization capability, a shape design based on NACA 0012 is conducted to obtain the optimal shape in view of propulsive efficiency. The design conditions are: $Re = 20,000$, $k = 1.07125$, $h_0 = 0.175$, and $\alpha = 0°$. As observed in Fig. 4, these conditions correspond to the highest peak of propulsive efficiency of the baseline NACA 0012, the shape optimization will attempt to further improve the maximum efficiency. The intermediate C-type grid (513x49) is used for the optimization, in view of balance between the computational accuracy and cost. Then, the performance and contours are obtained by using fine grid to evaluate improvement of the optimized design. Figure 12 shows the design history. The efficiency converged to 0.3157, an increase by 11% from 0.2844, while the thrust increases by 8.3% from 0.06205 to 0.06767 and power coefficient reduces by 1.8% from 0.2182 to 0.2143,

after about 33 design iterations. The profile of the optimized airfoil is compared with the NACA 0012 in Fig. 13. The key features of the geometrical change in the optimized airfoil are: the leading edge grows thicker and the trailing edge thinner than the baseline airfoil. It is noticeable that the resulted geometry is very similar to a tadpole-like airfoil, as suggested by Lee et al. [5]. In their parametric study, it was found that a thick leading edge is favorable for better propulsive efficiency in a relatively high-frequency flapping motion because a thick leading edge can reduce the strength of vortices generated there, which increases required power input. Regarding the trailing-edge shape, they suggested that a thinner airfoil could produce a larger pressure gradient between upper and lower surface, which in turn can generate stronger thrusting jets responsible for producing a positive net thrust force. The time histories of thrust coefficients by the baseline and optimized airfoils are compared in Fig. 14. Figure 14 shows that the symmetric geometry results in an almost identical thrust generation at up and down strokes (i.e., symmetry in C_t). The improvement performance by the optimized geometry is eminent at positive peaks in the thrust coefficient (e.g., about t=9.25T and 9.75T). Figures 15-17 suggest how the wake of the optimized airfoil differs from that of the NACA 0012. In the current design condition, the leading edge vortices (LEVs) flow down and interact with the trailing edge vortices (TEVs). It is observed that the LEV, as it convects downstream towards the trailing, leads to the formation of vortex pairs. For both airfoils, the wake vortex structures, after detaching from the trailing edge, show complicated patterns attributable to the LEVs. However, they eventually evolve to form the inverse Kármán vortices as the small vortex singlet and/or pairs are merged or dissipated as shown in Fig. 15. For a clear definition of wake trend, we shall use "S" to denote a single vortex and "P" to denote a pair of vortices of opposite signs [25]. Accordingly, in Fig. 16, the baseline airfoil shows a 6P+2S wake (3P+S at each stroke) pattern at the moment right after the vortices

are detached from the trailing edge. On the other hand, the optimized airfoil shows a 10P+2S wake pattern (5P+S at each stroke) temporarily. Consequently, the generation of 2 extra vortex pairs per stroke by the optimized airfoil enhances its thrusting performance.

The mechanism of improvement can be explained by the role of LEVs. On the baseline airfoil, two LEVs (A and B) flow down to the trailing edge at $t/T=9.5$ on the upper surface and at $t/T=10.0$ on the lower surface (C and D), respectively. The LEVs, A and C, originate in the very leading edge region and the others, B and D, near $x/c=0.25$, where the airfoil has maximum thickness, at around $t/T=9.35$ on the upper surface (see Fig. 15) and at about $t/T=9.85$ on the lower surface. With the shape change, the optimized airfoil gets thicker in the front section and the trailing edge becomes sharper. As observed in Figs. 15 and 16, the LEVs in B (see $t/T=9.5$) and D ($t/T=10$) become larger than those of baseline airfoil, while the LEVs in A ($t/T=9.75$) and C ($t/T=9.25$) get smaller. The strengthened LEVs B and D make a '2P' in the wake by interacting with TEVs, instead of a stretched 'P' in the baseline airfoil. As shown in Figs. 17, the vorticity contours and streamlines at $t/T=9.3$ indicate that '2P' structure of optimized airfoil is much more favorable than 'P' wake pattern of NACA 0012; the arrows in the figure indicate the velocity collectively generated by the pair at the neighboring boundary. It shows that addition of positive velocity has been achieved by the optimized airfoil, rather than cancellation in the case of NACA 0012. Thus, the effect of thrusting jet is maximized on the optimized airfoil by synchronizing generation of vortex pairs by the shape with the imposed flapping motion to yield a favorable wake field. Here, we define the favorable wake field as having thrust-inducing jet flows in which a counter-clockwise vortex is placed above the clockwise vortex so that the induced jet flow is directed towards the stream direction.

B. Shape Optimization for an Asymmetric Airfoil (SD7003)

Now we shall turn our attention to the designs of an asymmetric airfoil, SD7003, for a lift generating flight. The design conditions for shape and trajectory optimizations remain the same as those for validation study in Section IV-C: Re = 10,000, k = 3.93, h_0 = 0.05, but α = 8° allowing a higher lift force. The design history for maximizing propulsive efficiency with shape parameters is presented in Fig. 18. In less than 20 design iterations, the process has converged; the propulsive efficiency is increased by 14.2% from 0.1584 to 0.1809, and the thrust coefficient improved by 13.4% from 0.04605 to 0.05221. Both performance indicators have very similar convergence characteristics because the power input has kept within a very slight variation from the baseline geometry, decreasing from 0.2907 to 0.2886. For a further investigation of geometry, the airfoil profiles of the baseline and optimized geometries are compared in Fig. 19. The overall trend for shape change is very similar to those of previous case, i.e., a thickened leading edge and a sharpened trailing edge. In addition, the optimized airfoil shows a larger change on the lower surface than on the upper surface, resulting in a tadpole like shape. Figure 20 compares the time-histories of thrust coefficients of the optimized airfoil with that of SD7003 between t/T=18.0 and 20.0 (19th and 20th cycles). Besides the interval between t/T=19.4~19.75 (Δt/T=35%), the overall thrust generation increases. Especially, the thrust during down-stroke (t/T=19~19.4) is improved, primarily resulting from the change on the lower surface.

The unsteady patterns of vortices around the optimized airfoil at select physical time steps are compared with those of the baseline airfoil in Fig. 21. Overall, both of the airfoils produce similar inverse Kármán vortices wake pattern but the spaces between vortex cores (in both horizontal and vertical directions), which are generated at the same time interval, are wider on the optimized airfoil. Thus, it can be confirmed that the wake flow acceleration of the optimized

airfoil is stronger than that of the baseline. A close examination of Fig. 21 reveals that the strength of the LEV on the upper surface of the optimized airfoil is smaller than that of the baseline model. This reduces power input needed for generating those vortices. Besides, the TEV of the optimized airfoil, which are detached from the airfoil at the end of strokes (t/T=19.5, t/T=20.0), are more stretched with stronger intensity. As a result, the flow acceleration could be enhanced by the shape optimization. The x-momentum contours plotted at t/T=19.3 in Fig. 22 show that the optimized airfoil produces larger areas of high velocity in the wake vortices than the baseline airfoil. Further investigation about the optimized airfoil and the effect of trajectory design will be discussed in the following section.

C. Trajectory Optimization (SD7003)

Trajectory and geometric parameters can be considered together in the design of an MAV, where an instantaneous optimal combination of both parameters during the flight will be sought after. However, it is instructive to carry out separate optimizations for geometry and trajectory so that insight into individual effects can be gained, prior to taking both into account. In our trajectory optimization, the reduced frequency and plunging amplitudes will be fixed for each optimization; but they will be varied when off-design performances are studied.

Through the trajectory optimization, the thrust coefficient increases from 0.04605 to 0.08099, a remarkable 75.8% increase with respect to the baseline, as displayed in Fig. 23. However, the propulsive efficiency increases by 7.3% only, from 0.1586 to 0.1701, because the change of motion parameters increases not only the thrust force but also the power input. The final design parameters after optimization are presented in Table 1. The design parameters that have larger changes than the others are selected for presentation. The major change comes from not only low frequency ($m = 1$), which is same as the baseline motion, but also from higher frequencies ($m = 2$

and 5), which lead to a more oscillatory motion. Figure 24 compares trajectories of the baseline and optimized motions; the optimized trajectory is noted for its asymmetrical behavior, while modulating the baseline motion with small amplitude oscillations of higher harmonics. The effect of higher harmonics is more noticeable during down stroke. The vorticity contours at select physical time steps are compared in Fig. 25. Even though the wavy motion generates many small vortex pairs ('P') or singlets ('S') during a cycle, it still results in '2S' inverse Kármán vortices similarly to the baseline harmonic motion overall. However, the distance between positive and negative vortex cores is wider and the size of vortices is much larger than those in the harmonic motion. The oscillatory motion spread the small vortices in a wider wake area, which eventually merge together to form a larger '2S' wake. Investigating closely, several jet producing vortex pairs are generated even in one excursion from top to bottom of the motion, especially at the phase from t/T=19.25 to 19.75. Those vortices are shed at the phase from t/T=19.75 to 20.25 (same as 19.25). Thus, most of the thrust force is generated at the phase from t/T = 19.25 to 19.75, so is in the baseline motion, but the wavy motion generates the thrust more intermittently, thereby producing more of thrust-favoring vortices. This mechanism is more clearly observed in Fig. 26, in which the time-varying and time-averaged thrust coefficients at sub-intervals for both the baseline and optimized motions are shown. The sub-interval of time-averaged values is taken to be 0.1T, corresponding to the smallest period (highest frequency mode). The added high-frequency components increase the overall amplitude of thrust coefficient. The maximum thrust coefficient reaches about 3.4 instantly, about 10 times that (0.35) of the baseline motion. While the wavy motion causes large-amplitude fluctuations in thrust, the end result is that a significant thrust generation over a period. As clearly revealed in Fig. 26, the major gain in thrust happens during t/T = 19.10–19.40, especially 19.30–19.40, in

which the peak value in the optimized motion is more than doubled. It is noted that the thrust generation occurs during the down stroke phase (t/T=19.0–19.5) and during the beginning of up stroke (19.5–19.75) in both baseline and optimized motions. The thrust generating mechanism of the optimized motion can be explored by investigating the vortex structures around the trailing edge at select peak of thrust during this positive net thrust phase, as displayed in Figs. 27. The baseline motion generates '2S' wakes consistently while those of the optimized motion evolve dynamically. Also, the streamline patterns in the optimized motion, reflecting the vortex strength and direction, suggests a wider jet flow area than the baseline motion does. Furthermore, small 'P's and 'S's in the trailing edge region enhances the wake velocity components in the streamwise direction, especially at t/T=19.125 and 19.325, when two highest peaks of thrust are observed. To give a succinct comparison of effectiveness of applying optimization, the time-averaged performances of the shape-optimized, trajectory-optimized, and baseline models are presented in Table 2. The trajectory optimization doubles the thrust of the baseline motion and is significantly higher than the shape optimization; its lift force however deteriorates by about 1.7% and 2.5% in comparison with the baseline and shape optimization respectively. To sustain the motion, the power input needs to be increased, thereby resulting in a not as high an increase in thrust, but still a significant improvement, 11% and 7.3% respectively by the shape and trajectory optimizations.

As impressive as it may be, it begs the question as to how well the optimized configurations (airfoil shape and trajectory) described above will perform at off-design conditions, as shall be discussed in what follows.

D. Off-design conditions

The performances of optimized geometry and trajectory are investigated at various values of *kh* by varying reduced frequency *k* from 1.965 to 15.75 (*k*=3.93 is the design condition). Figures 28 show the overall efficiency and thrust performance vs. *kh* for four cases: a combination of baseline and optimized shape and trajectory; all are computed at the same angle of attack of 8° and Reynolds number of 10,000. Recall that the baseline airfoil is denoted as SD7003. It is noted that the in the fourth case, it is assumed that the optimal trajectory obtained for the baseline airfoil maintains its high performance for the optimized airfoil.

In Fig. 28-(a), the optimized airfoil gives a superior performance to the baseline airfoil at almost all of the conditions. Especially, the maximum efficiency is improved from 18.45% at *kh* = 0.2260 (baseline) to 22.1% at *kh* = 0.2555(optimized); the optimized airfoil surpasses the baseline in efficiency in the entire range of *kh*. The thrust coefficients of the optimized geometry are also higher than those of baseline except when 0.4 < *kh* < 0.55 where the SD7003 airfoil shows unusual pattern in efficiency and thrust coefficient. It is reported that the efficiency curves of flapping airfoils have only one extrema in the *kh* space [23], but SD7003 has two; this behavior is correlated with that in the thrust coefficient curve, in which it exhibits a reflection point. This peculiarity disappears in the optimized airfoil. Moreover, the optimized airfoil in baseline motion shows a superior performance to that by the baseline airfoil in optimized trajectory, except in the low flapping speed regime, 0.14 < *kh* < 0.21, as evident in the amplified view displayed in Fig. 28-(b). In this figure, the best performer belongs to the optimized shape with the optimized trajectory. These results suggest that the trajectory optimization should be carefully carried out via a more rigorous design formulation in which both the shape and trajectory optimizations are carried out simultaneously. That is, the interaction between

geometrical and dynamical (via trajectory of motion) factors may not be negligible if a more robust optimization is sought after. Nevertheless, the present study already shows that the geometric optimization obtained at one design point is shown to be sufficiently robust that its superiority in performance persists in all off-design points.

VI.   Conclusion

Optimal designs for airfoil shape and flight trajectory under periodic flapping motion have been conducted by using the unsteady discrete adjoint approach in which time-averaged objective functions are considered with periodic conditions applied to flow derivatives and adjoint vectors. Accurate solutions of sensitivities have been obtained with this approach in an iterative manner. With the adjoint approach described here, optimization of unsteady problems that contain a large number of design variables can be solved within a practically acceptable time frame. For flapping airfoil problems, improvements for the thrust and propulsive efficiency were achieved by shaping airfoil and/or changing the motion trajectory.

Design optimizations are conducted for shape designs of symmetric (NACA 0012) and asymmetric (SD7003) airfoils and a trajectory design. NACA 0012 is re-designed at its best efficiency point (kh=0.187) to improve the maximum efficiency. The propulsive efficiency is improved by 11% and the thrust increases by 8.3% and the power coefficient reduced by 1.8%. The improvement in the propulsive efficiency comes from higher thrust and lower aerodynamic work; the former originates from the sharpened trailing edge and the latter from the thickened leading edge..

For further practical applications, i.e., optimization of lift-generating airfoil shape for plunging motion and its trajectory are carried out based on SD7003. Trajectory optimization produces an increase in thrust by 76%. As more power input to sustain the maneuvering of the

optimized motion is required, the improvement in the propulsive efficiency is about 7.8%. On the other hand, although the shape optimization increases the thrust force by just 13.4%, it produces a higher propulsive efficiency than the trajectory optimization because the power input remains almost unchanged with the shape. In addition, the study of off-design conditions showed the shape-optimized airfoil is quite robust that its performance is almost always superior to that of the baseline airfoil. This finding suggests that shape optimization could be very useful for designing aerodynamically efficient bio-inspired MAVs, when constrained by conditions, such as limit of power input or trajectory prescribed by an actuator or given mission. In the optimal design of trajectory, it is observed that the effect of oscillatory non-harmonic motion is to shift the frequency of motion instantaneously so as to find a locally better performance.

Acknowledgments

References

[1] Lai, J. C. S. and Platzer, M. F., "The Jet Characteristics of a Plunging Airfoil," *AIAA Journal*, Vol. 37, No. 12, Dec. 1999, pp. 1529–1537.
doi: 10.2514/2.641

[2] Jones, K. D., Dohring, C. M., and Platzer, M. F., "An Experimental and Computational Investigation of the Knoller-Beltz Effect," *AIAA Journal*, Vol. 36, No. 7, 1998, pp. 1240–1246.
doi: 10.2514/2.505

[3] Anderson, J.M., Streitlen, K., Barrett, D. S., and Triantafyllou, M. S., "Oscillating Foils of High Propulsive Efficiency," *Journal of Fluid Mechanics*, Vol. 360, 1998, pp. 41–72.

doi: 10.1017/S0022112097008392

[4] Schouveiler, L., Hover, F. S., and Triantafyllou, M. S., "Performance of Flapping Foil Propulsion," *Journal of Fluids and Structures*, Vol. 20, No. 7, Special Issue, Oct. 2005, pp. 949–959.

doi: 10.1016/j.jfluidstructs.2005.05.009

[5] Lee, J. S., Kim, C., and Kim, K. H., "Design of Flapping Airfoil for Optimal Aerodynamic Performance in Low-Reynolds Number Flows," *AIAA Journal*, Vol. 44, No. 9, 2006, pp. 1960–1972.

doi: 10.2514/1.15981

[6] Tuncer, I. H. and Kaya, M., "Optimization of Flapping Airfoils For Maximum Thrust and Propulsive Efficiency," *AIAA Journal*, Vol. 43, Nov. 2005, pp. 2329–2341.

doi: 10.2514/1.816

[7] Kaya, M. and Tuncer, I. H., "Optimization of Flapping Motion Parameters for Two Airfoils in a Biplane Configuration," *Journal of Aircraft*, Vol. 46, No. 2, 2009, pp.583–592.

doi: 10.2514/1.38796

[8] Kim, C. S., Kim, C., and Rho, O. H., "Feasibility Study of Constant Eddy-Viscosity Assumption in Gradient-Based Design Optimization," *Journal of Aircraft*, Vol. 40, No. 6, 2003, pp.1168–1176.

[9] Lee, B. J. and Kim, C., "Aerodynamic Redesign using Discrete Adjoint Approach on Overset Mesh System," *Journal of Aircraft*, Vol. 45, No. 5, 2008, pp.1643–1653.

doi: 10.2514/1.34112

[10] Leoviriyakit, K. and Jameson, A., "Multi-point Wing Planform Optimization via Control Theory," 43rd AIAA Aerospace Sciences Meeting & Exhibit, AIAA Paper 2005-0450, January 2005, Reno, NV, USA.

[11] Heathcote, S. and Gursul, I., "Jet Switching Phenomenon for a Periodically Plunging Airfoil," *Physics of Fluids*, Vol. 19, No. 2, 2007.

doi: 10.1063/1.2565347

[12] Cleaver, D. J., Wang, Z., and Gursul, I., "Vortex Mode Bifurcation and Lift Force of a Plunging Airfoil at Low Reynolds Numbers," 48th AIAA Aerospace Sciences Meeting including the New Horizons Forum and Aerospace Exposition, AIAA Paper 2010-390, January 2010, Orlando, FL, USA.

[13] Vytla, V. V., Huang, P. G., and Watanabe, N., "Simulation of Low Reynolds Number Airfoil Subjected to High Frequency Pitch/Plunge," 19th AIAA CFD Conference, AIAA Paper 2009-4272, June 2009, San Antonio, TX, USA.

[14] Nadarajah, S. and Jameson, A., "Optimal Control of Unsteady Flows using Time Accurate and Non-Linear Frequency Domain Methods," 9th AIAA/ISSMO Symposium on Multidisciplinary Analysis and Optimization Conference, AIAA Paper 2002-5547, September 2002, Atlanta, GA, USA.

[15] Krakos, J. A. and Darmofal, D. L., "Effect of Small-Scale Unsteadiness on Adjoint-based Output Sensitivity," 19th AIAA CFD Conference, AIAA Paper 2009-4274, June 2009, San Antonio, TX, USA.

[16] Yamaleev, N. K., Diskin, B., and Nielsen, E. J., "Local-in-time Adjoint-based Method for Design Optimization of Unsteady Compressible Flows," 47th AIAA Aerospace Sciences Meeting and Exhibition, AIAA Paper 2009-1169, January 2009, Orlando, FL, USA.

[17] Hirsch, C., *Numerical Computation of Internal and External Flows Vol.2: Computational Methods for Inviscid and Viscous Flows*, WILEY, 1984, 1st Ed., Ch. 23.

[18] Hicks, R. M. and Henne, P. A., "Wing Design by Numerical Optimization," *Journal of Aircraft*, Vol. 15, No. 7, 1978, pp. 407– 412.

doi: 10.2514/3.58379

[19] http://www.ae.uiuc.edu/m-selig/ads/coord_database.html

[20] Ol and Michael, "Vortical Structures in High Frequency Pitch and Plunge at Low Reynolds number," 37th AIAA Fluid Dynamics Conference and Exhibit, AIAA Paper 2007-4233, Miami, FL, June , 2007.

[21] McGowan, Gregory, Gopalarathnam, Ashok, Ol, Michael, Edwards, Jack, and Fredberg, and Daniel, "Computation vs. Experiment for High-Frequency Low-Reynolds Number Airfoil Pitch and Plunge," 46th AIAA Aerospace Sciences Meeting and Exhibit, AIAA-Paper 2008-653, Reno, NV, January, 2008.

[22] Press, W. H., Flannery, B. P., Teukolsky, S. A. and Vetterling, W.T., *Numerical Recipes in FORTRAN 77: The Art of Scientific Computing (V. 1)*, Cambridge University Press, 2nd Ed., 1992.

[23] Young, J. and Lai, J. C. S., "Mechanisms Influencing the Efficiency of Oscillating Airfoil Propulsion," *AIAA Journal*, Vol. 45, No. 7, July 2007.

[24] Y. Lian and W. Shyy, "Aerodynamics of Low Reynolds Number Plunging Airfoil under Gusty Environment," 45th AIAA Aerospace Science Meeting and Exhibit, AIAA-Paper 2007-71, Reno, NV, January, 2007.

[25] Schnipper, Andersen and Bohr, "Vortex wakes of a flapping foil," *Journal of Fluid Mechanics*, Vol. 633, pp. 411-423, 2009.

Tables

Table 1 Motion parameters for trajectory-optimized case

(Select sinusoidal parameters, design condition: Re = 10,000, k = 3.93, h_0 = 0.05, α = 8°)

Parameters	Index of design variable	Baseline	Trajectory optimized
$\beta_1 \sin(2\pi fr_h t)$	1	0.0	5.1736E–03
$\beta_2 \cos(2\pi fr_h t)$	2	0.0	–8.3726E–04
$\beta_3 \sin(4\pi fr_h t)$	3	0.0	–1.4634E–03
$\beta_4 \cos(4\pi fr_h t)$	4	0.0	1.1642E–03
$\beta_9 \sin(10\pi fr_h t)$	9	0.0	–1.4559E–03
$\beta_{10} \cos(10\pi fr_h t)$	10	0.0	1.9877E–03

Table 2 Comparison of performances

(Design condition: Re = 10,000, k = 3.93, h_0 = 0.05, α = 8°)

Performance	Baseline	Shape optimized	Trajectory optimized
C_t	4.6047E–02	5.2213E–02	8.0991E–02
C_l	7.0569E–01	7.1178E–01	6.9392E–01
η	15.84%	18.09%	17.01%

Figures
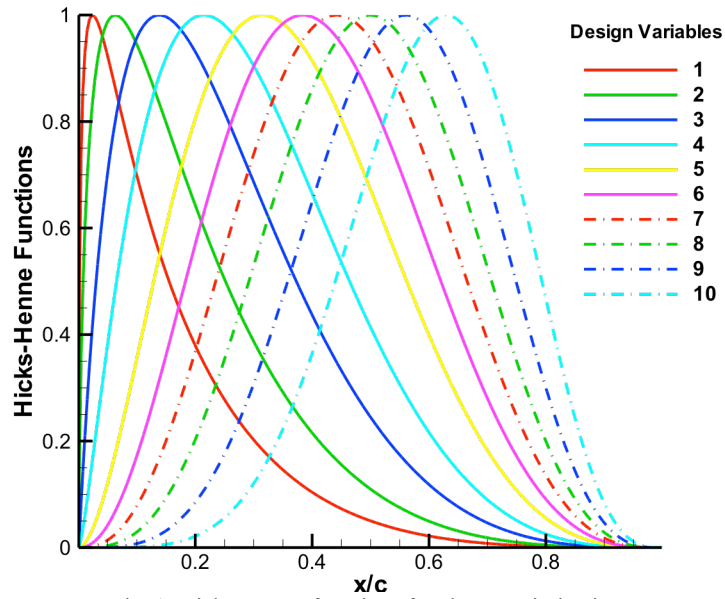
Fig. 1. Hicks-Henne functions for shape optimization
[same 10 functions are imposed on upper and lower surfaces]
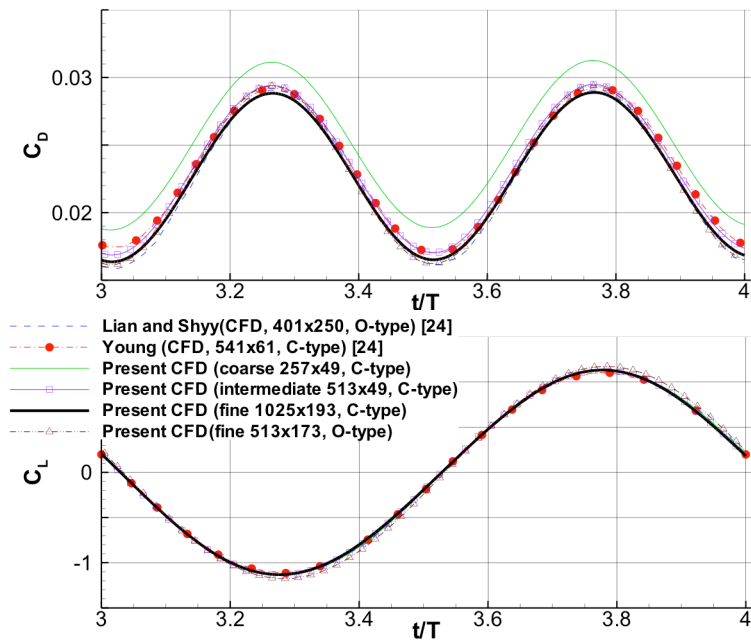
Fig. 2. Drag and lift coefficient history
[Re = 20,000, k = 3.93, h_0 = 0.0125, α = 0°, NACA 0012, harmonic motion]
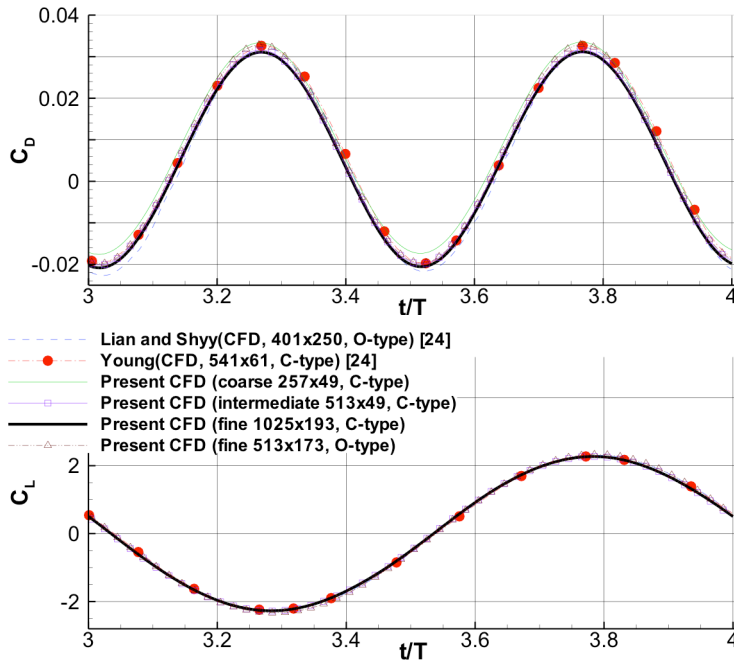
Fig. 3. Drag and lift coefficient history
[$Re = 20{,}000$, $k = 3.93$, $h_0 = 0.025$, $\alpha = 0°$, NACA 0012, harmonic motion]
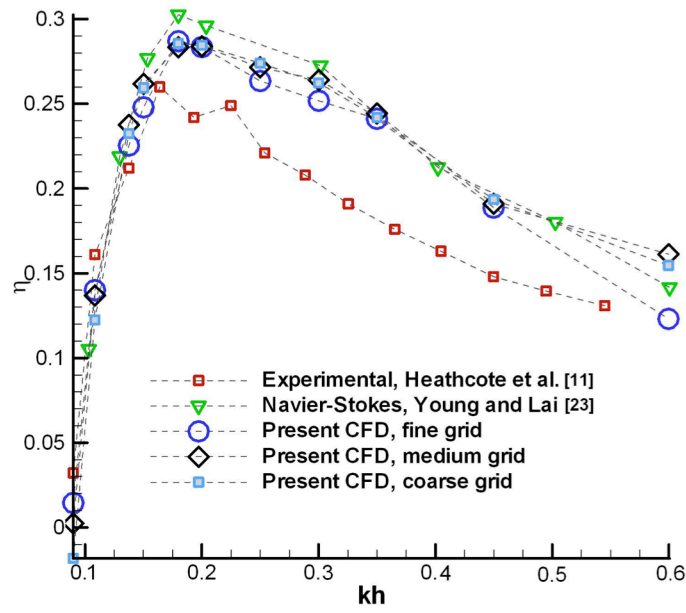
Fig. 4. Flow analysis and validation for pure plunging motion. Comparison of propulsive efficiency at various flapping conditions with experimental and numerical results for the time averaged performance. [NACA 0012, C-type, $Re = 20{,}000$, $h_0 = 0.175$, $k = \pi f r_h c / U_\infty$, kh corresponds to half of those in [11,23]]
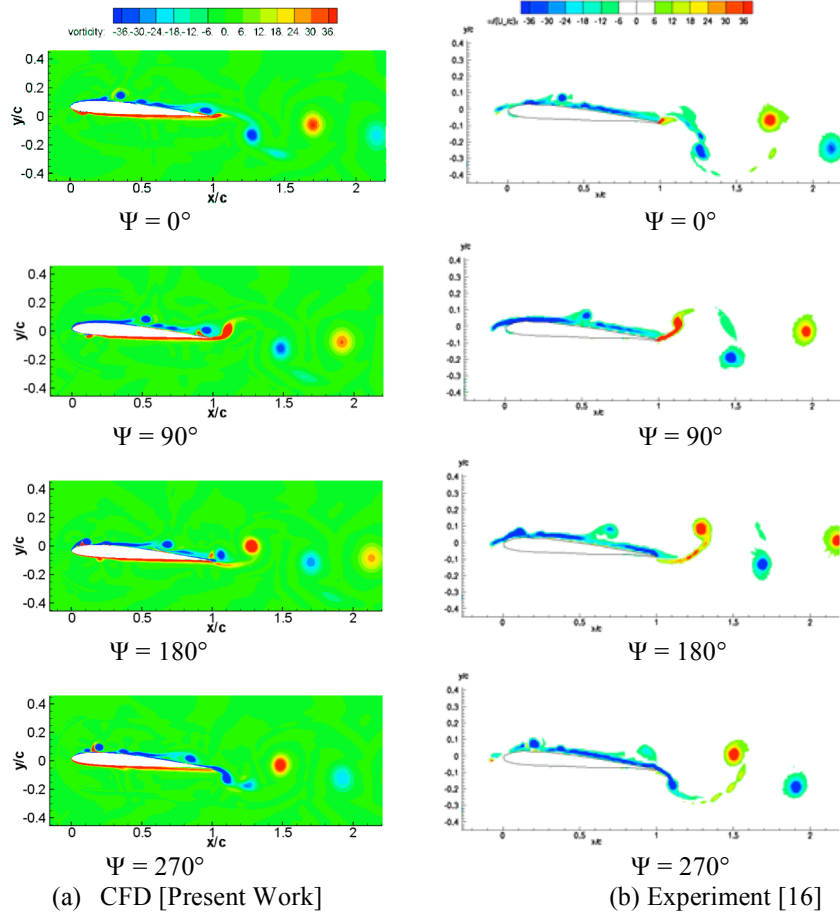
Fig. 5. Comparison of vorticity contours between (a) CFD and (b) experiment for pure plunging motion
[Re = 10,000, k = 3.93, h_0 = 0.05, α = 4°, harmonic motion, CFD: 20th cycle, fine grid, experiment: phase-averaged
PIV for 120 periods]

$\Psi = 0°$

$\Psi = 90°$

$\Psi = 180°$

$\Psi = 270°$
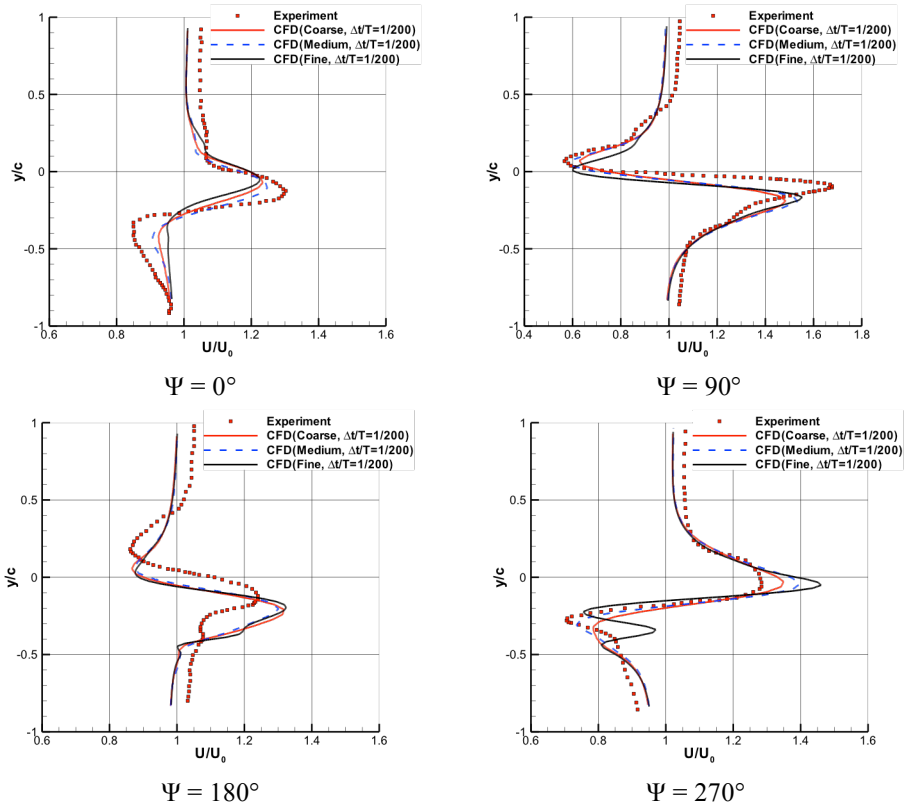
Fig. 6. Grid refinement study of wake profile validation
[$Re = 10,000$, $k = 3.93$, $h_0 = 0.05$, $\alpha = 4°$, harmonic motion,
experiment: phase-averaged PIV for 120 periods, CFD: 20th cycle, fine grid]

$\Psi = 0°$

$\Psi = 90°$

$\Psi = 180°$

$\Psi = 270°$
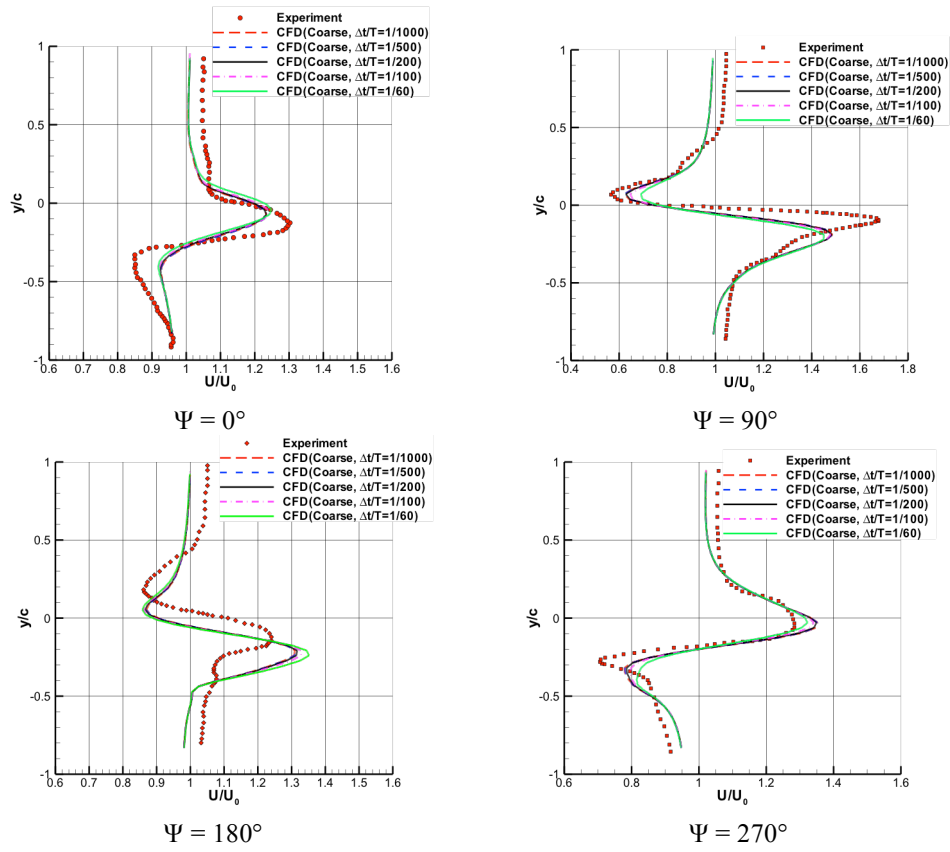
Fig. 7. Parametric study of wake profile validation based on the physical time step size
[$Re = 10,000$, $k = 3.93$, $h_0 = 0.05$, $\alpha = 4°$, harmonic motion,
experiment: phase-averaged PIV for 120 periods, CFD: 20th cycle, fine grid]
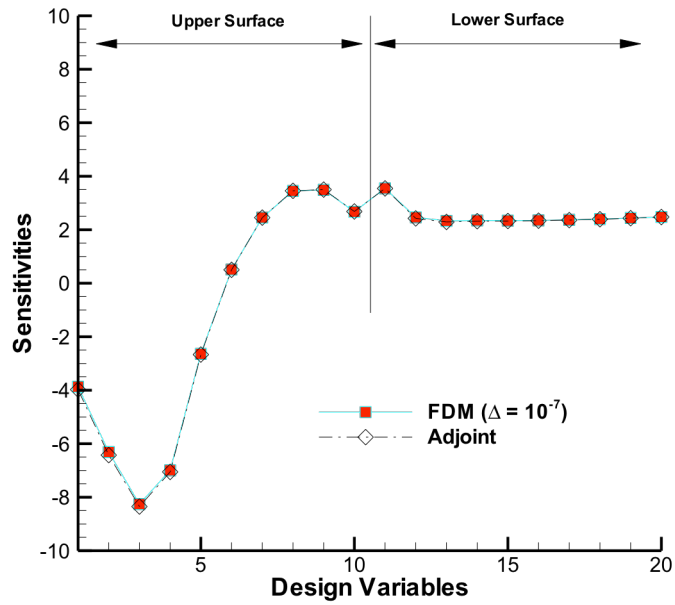
Fig. 8. Sensitivity analysis for lift coefficient with respect to shape parameters.
[SD7003, Re=10,000, α = 5°]
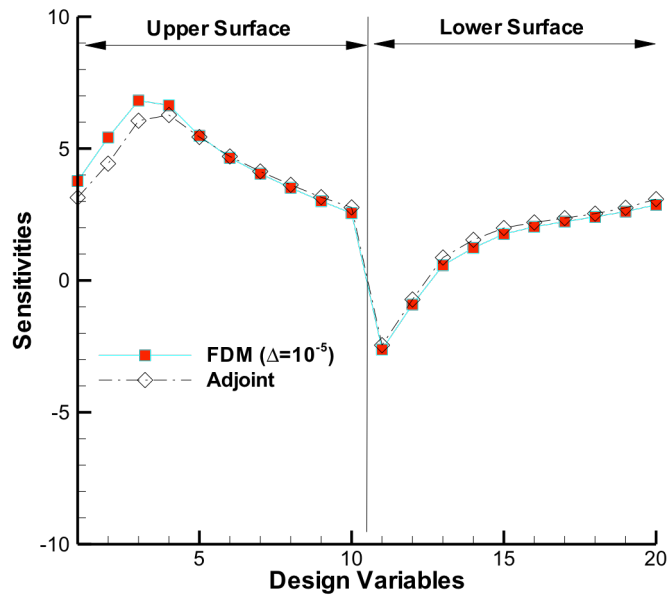
Fig. 9. Sensitivity analysis for time-averaged lift coefficient with respect to shape parameters ($\varepsilon = 10^{-4}$).
[SD7003, Re=10,000, k =3.93, h_0 = 0.05, α = 4°]
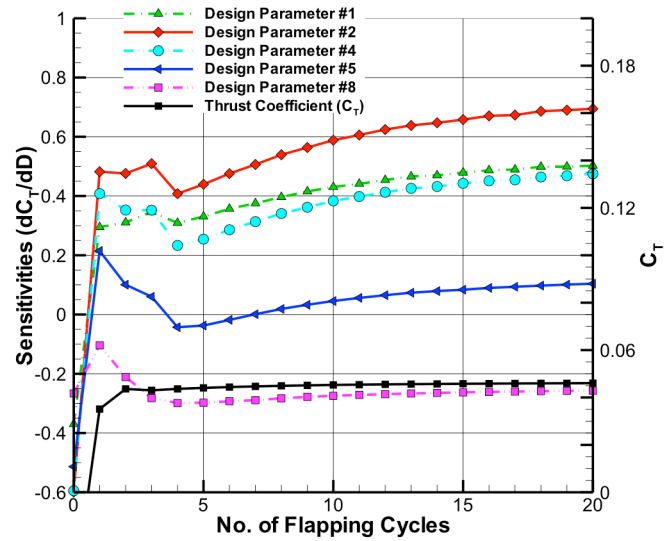
Fig. 10. Convergence history of time-averaged thrust coefficient and its finite differenced sensitivities with respect to shape parameters. [SD7003, Re=10,000, k =3.93, $h_0 = 0.05$, $\alpha = 4°$]
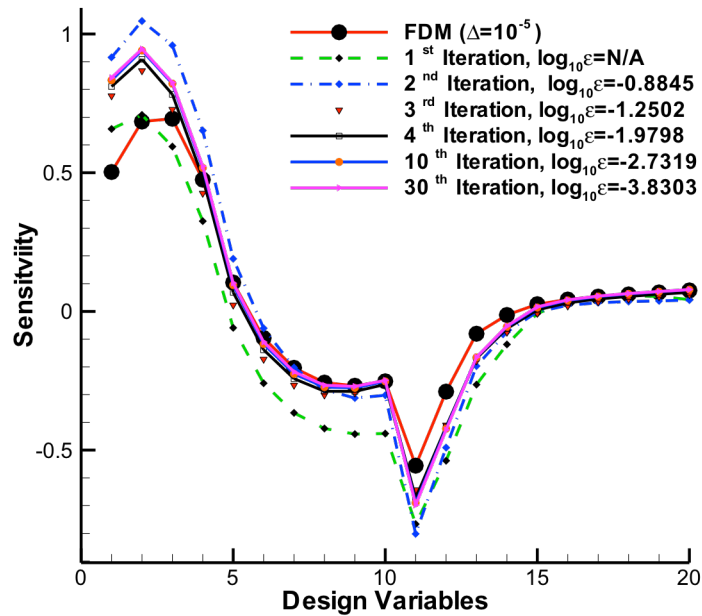
Fig. 11. Convergence of the sensitivities according to the number of outer iteration (time-averaged thrust coefficient, shape parameters). [SD7003, Re=10,000, k =3.93, $h_0 = 0.05$, $\alpha = 4°$]
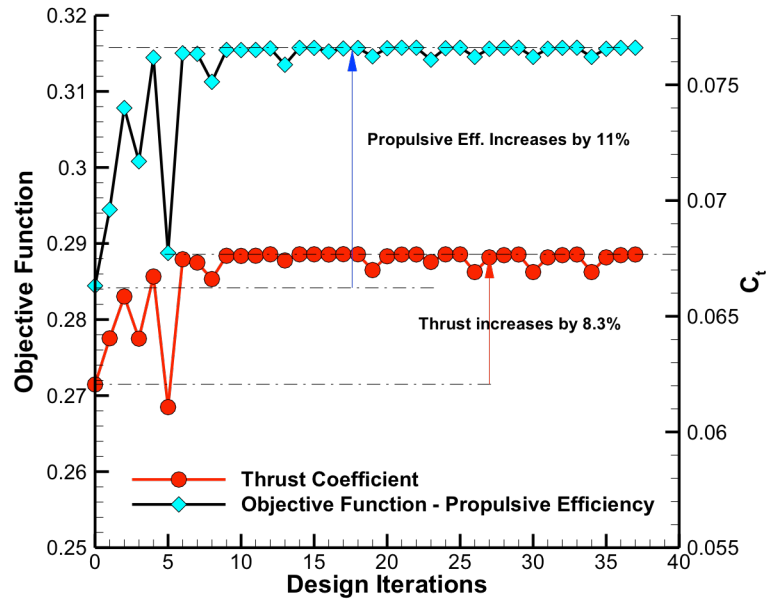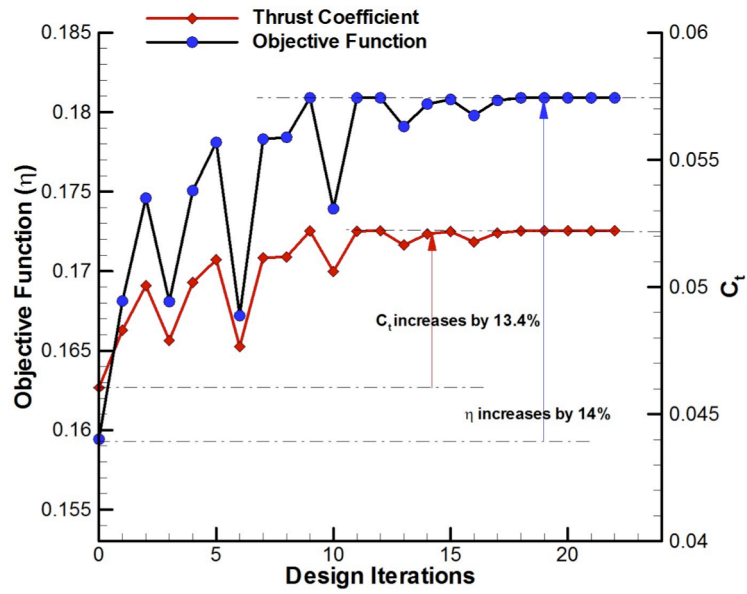
Fig. 12. Design history for maximizing propulsive efficiency with shape parameters.
[Re = 20,000, k = 1.0712, h_0 = 0.175, α = 0°, Baseline: NACA 0012]
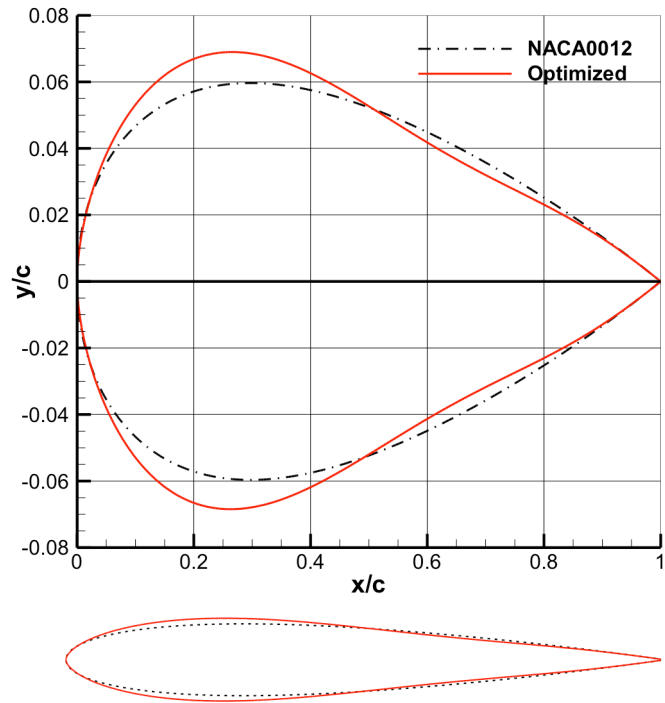
Fig. 13. Design history for maximizing propulsive efficiency with shape parameters.
[Re = 20,000, k = 1.0712, h_0 = 0.175, α = 0°]
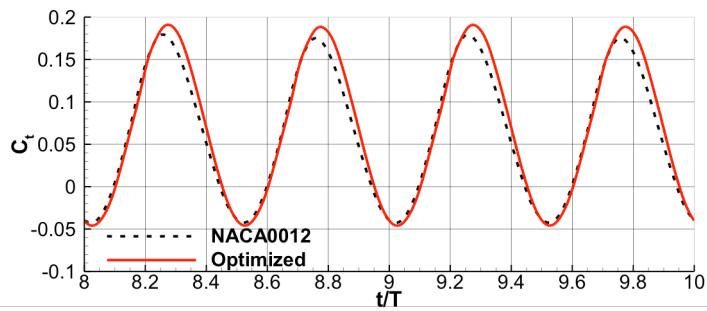
Fig. 14. The comparison of time-history of thrust coefficient [two periods, Re = 20,000, k = 1.0712, h_0 = 0.175, α = 0°, shape optimization, fine grid]

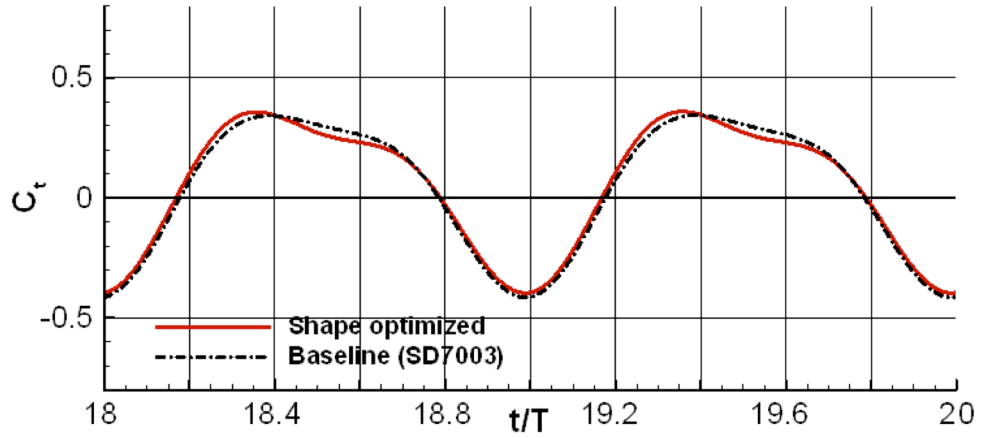**(a) NACA 0012**
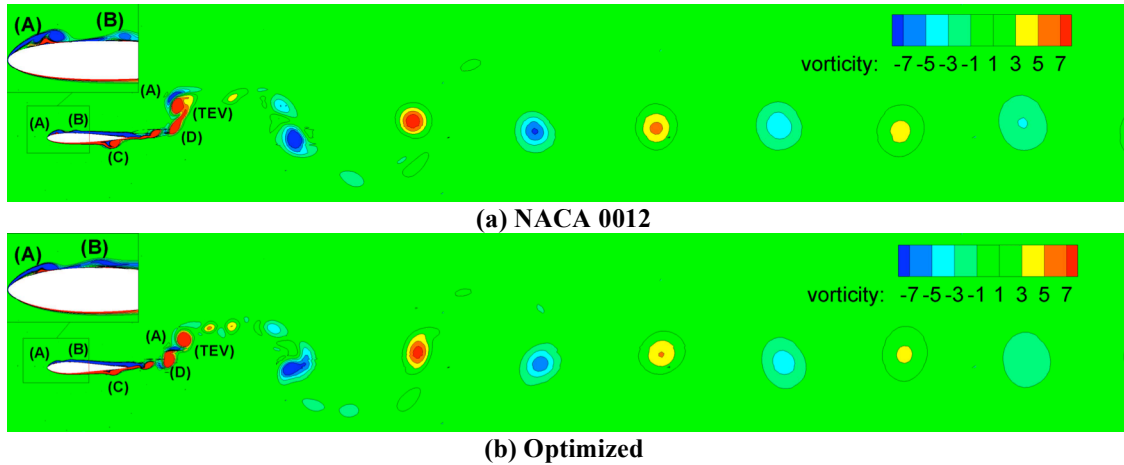
(b) Optimized

Fig. 15. Comparison of vorticity contours between baseline and optimized geometry for harmonic motion
[Re = 20,000, k = 1.0712, h_0 = 0.175, α = 0°, 10th cycle (t/T=9.325), shape optimization, fine grid]

t/T=9.25

t/T=9.5

t/T=9.75

t/T=10.0

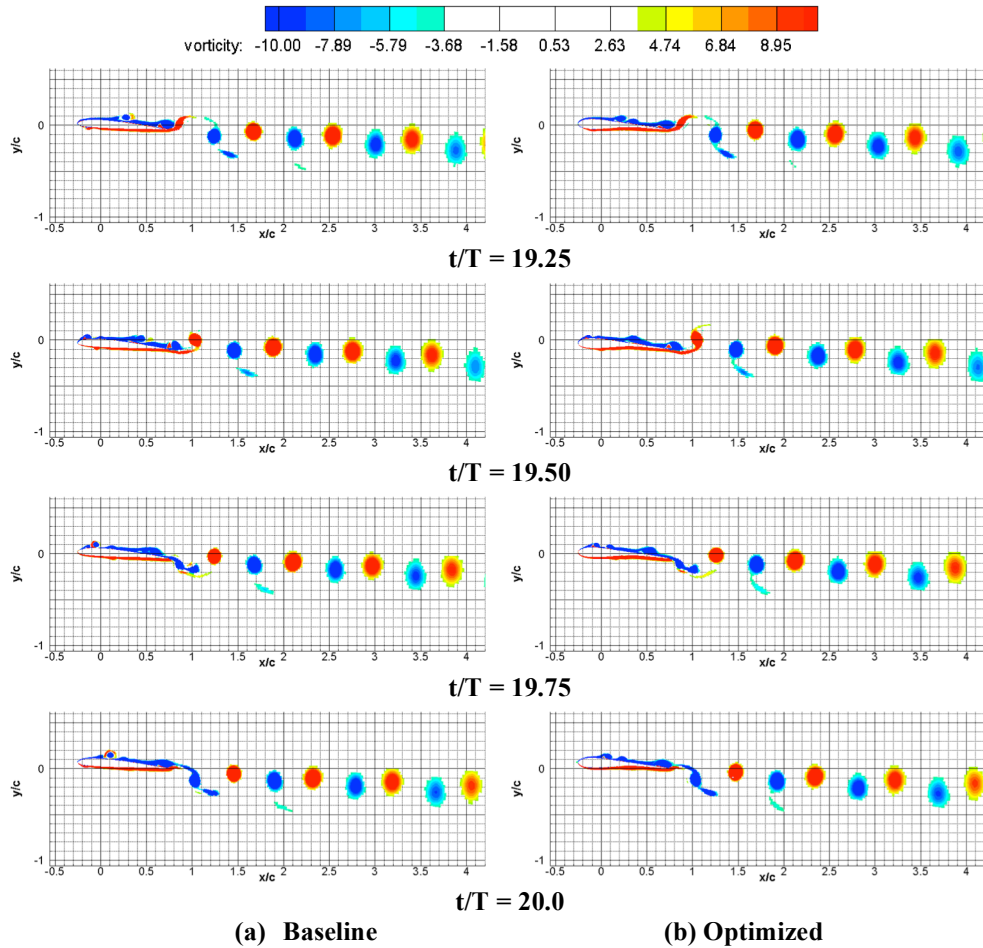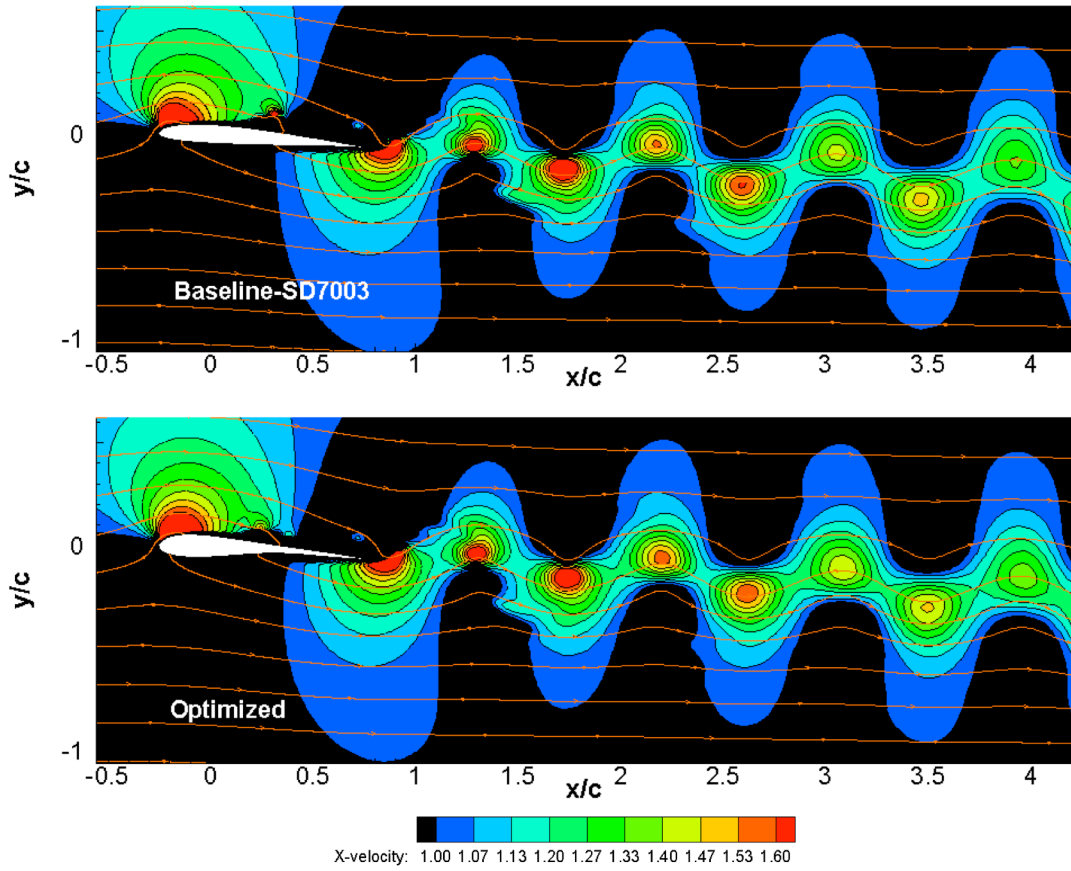**(a) NACA 0012**　　　　　　　　　　　**(b) Optimized**
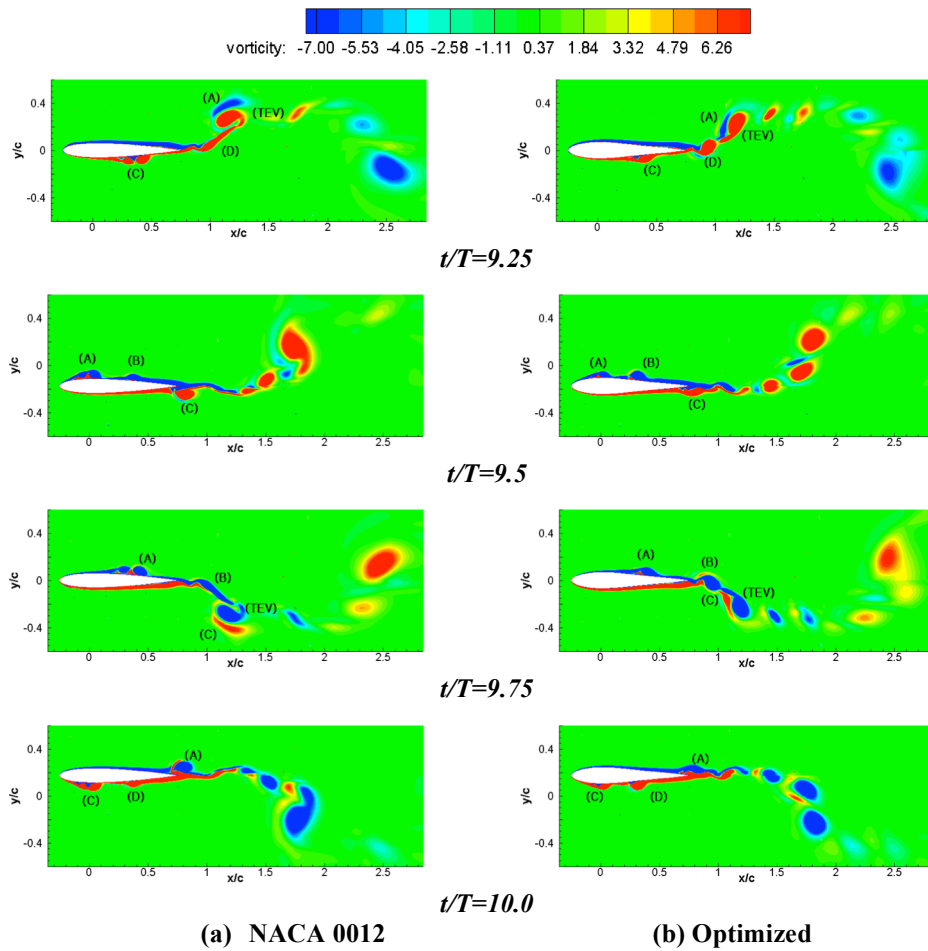
Fig. 16. Comparison of vorticity contours between baseline and optimized geometry for harmonic motion
[Re = 20,000, k = 1.0712, h_0 = 0.175, α = 0°, 10th cycle, shape optimization, fine grid]

(a) **NACA 0012**

→ Jet Driection
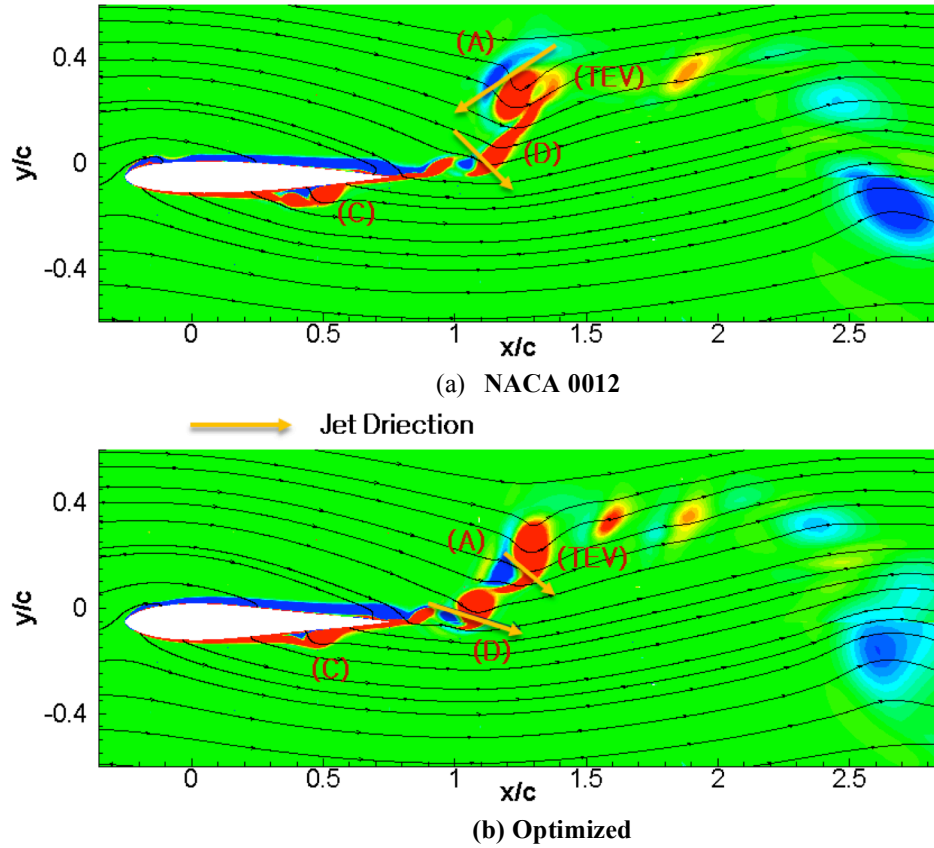
(b) Optimized

Fig. 17. Comparison of vorticity contours and streamlines between baseline and optimized geometry for harmonic motion [Re = 20,000, k = 1.0712, h_0 = 0.175, α = 0°, t/T=9.3, shape optimization, fine grid]
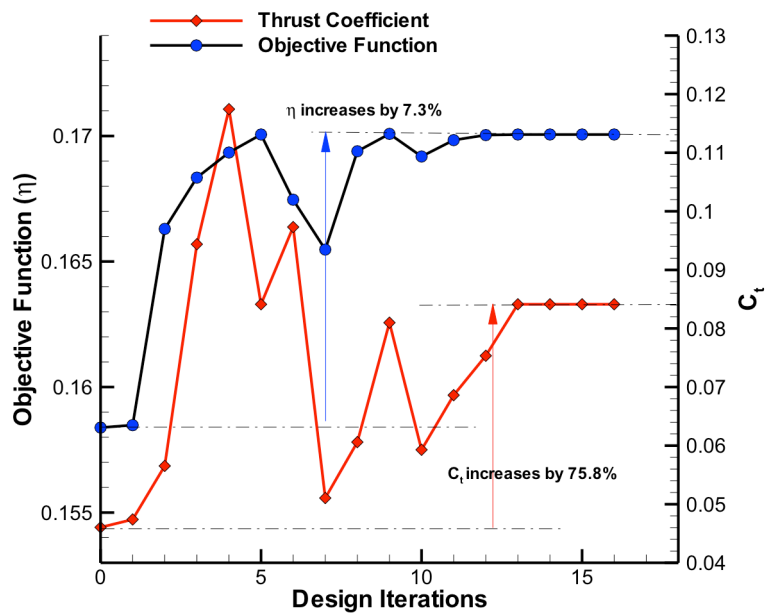
Fig. 18. Design history for maximizing propulsive efficiency with shape parameters.
[$Re = 10{,}000$, $k = 3.93$, $h_0 = 0.05$, $\alpha = 8°$, Baseline: SD7003]
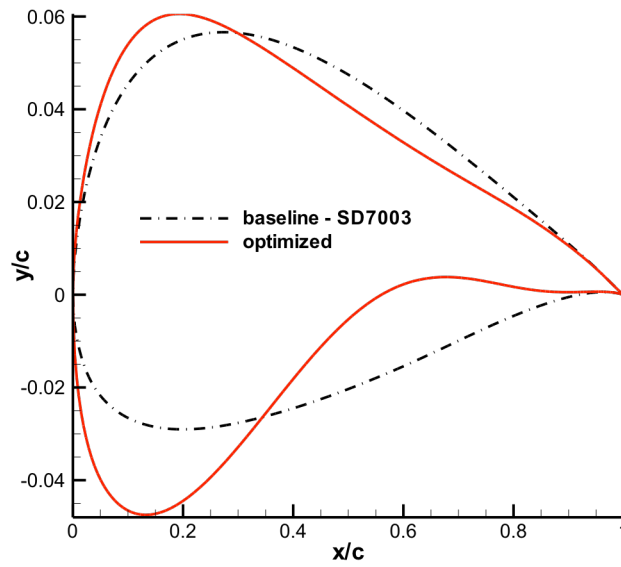
(a) Coordinates of airfoil profiles

(b) Shape of airfoils

Fig. 19. Comparison of airfoil shape between baseline and optimized geometries.
[$Re = 10{,}000$, $k = 3.93$, $h_0 = 0.05$, $\alpha = 8°$, Baseline: SD7003]

Fig. 20. Comparison of vorticity contours between baseline and optimized geometry for harmonic motion
[$Re = 10,000$, $k = 3.93$, $h_0 = 0.05$, $\alpha = 8°$, 19th and 20th cycles, shape optimization, fine grid]

t/T = 19.25

t/T = 19.50

t/T = 19.75

t/T = 20.0

(a) Baseline   (b) Optimized

Fig. 21. Comparison of vorticity contours between baseline and optimized geometry for harmonic motion
[$Re = 10,000$, $k = 3.93$, $h_0 = 0.05$, $\alpha = 8°$, 20th cycle, shape optimization, fine grid]

Fig. 22. Comparison of X-momentum contour between baseline and optimized geometry for harmonic motion
[$Re = 10{,}000$, $k = 3.93$, $h_0 = 0.05$, $\alpha = 8°$, t/T=19.3 cycle, shape optimization, fine grid]

Fig. 23. Design history for maximizing propulsive efficiency
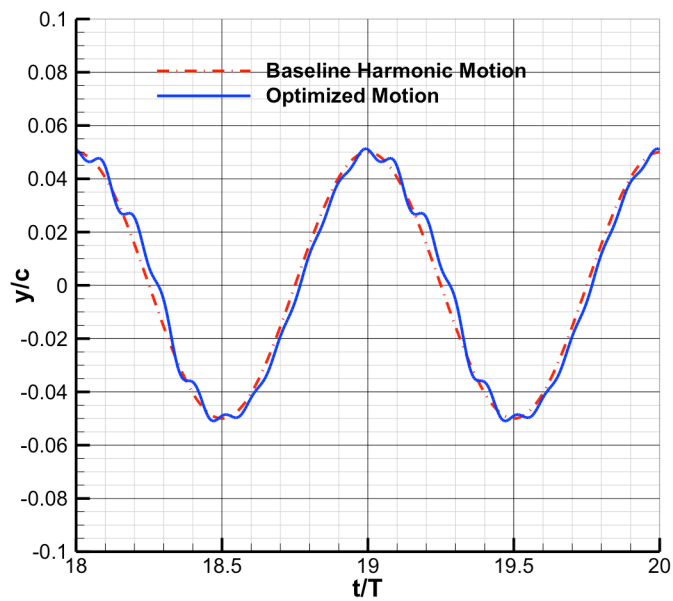with motion parameters. [$Re = 10,000$, $k = 3.93$, $h_0 = 0.05$, $\alpha = 8°$]

Fig. 24. Comparison of trajectory for two periods of flapping motion.
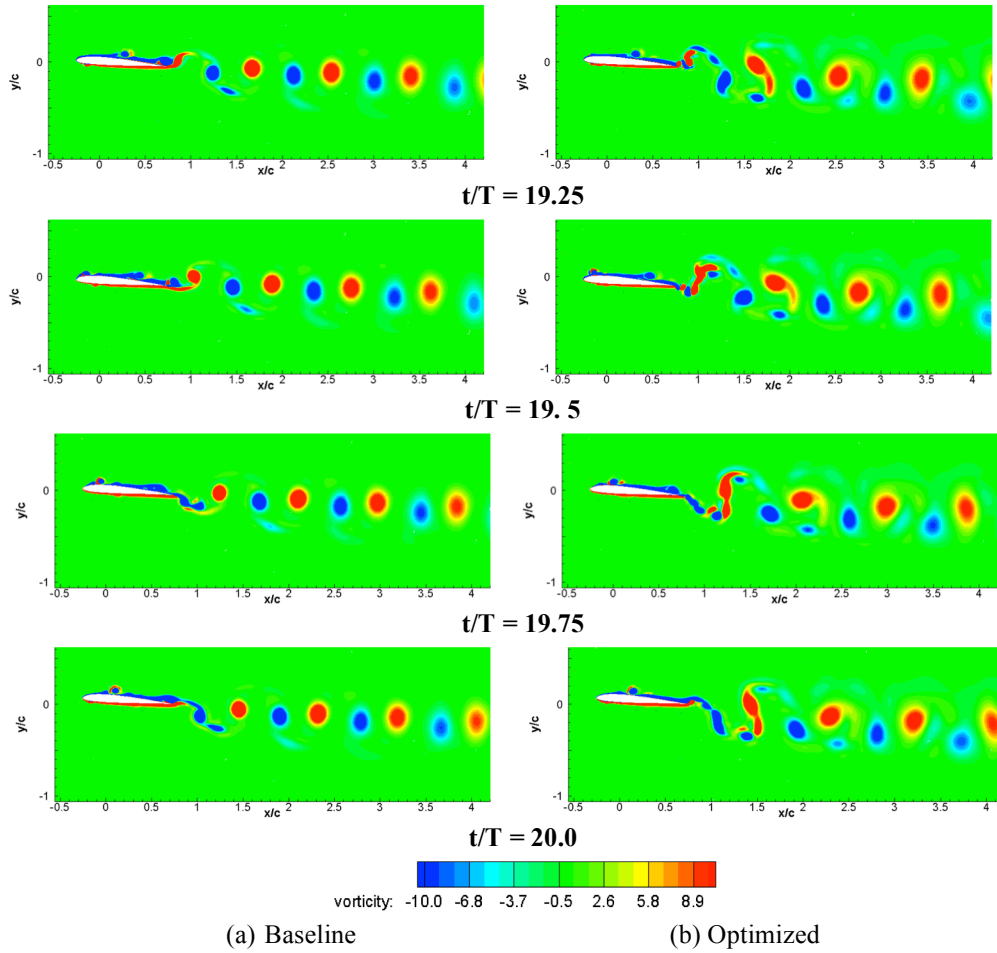[$Re = 10,000$, $k = 3.93$, $h_0 = 0.05$, $\alpha = 8°$]

t/T = 19.25

t/T = 19. 5

t/T = 19.75

t/T = 20.0

vorticity: -10.0 -6.8 -3.7 -0.5 2.6 5.8 8.9

(a) Baseline   (b) Optimized

Fig. 25. Comparison of vorticity contours between (a) baseline and (b) optimized geometry
[$Re = 10,000$, $k = 3.93$, $h_0 = 0.05$, $\alpha = 8°$, 20th cycle, trajectory optimization, fine grid]
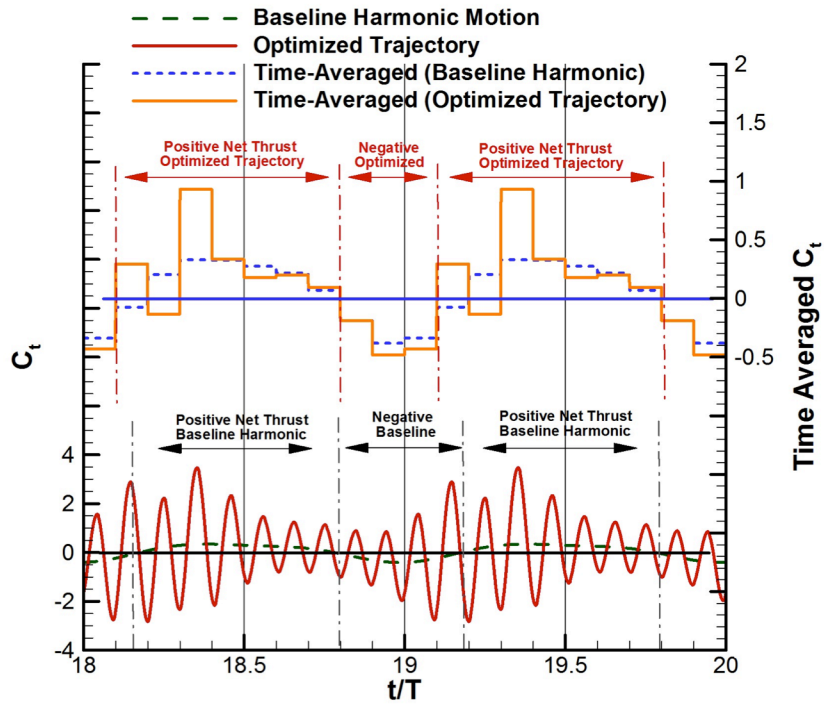
Fig. 26. Comparison of aerodynamic coefficients according to physical time step.
The sub-intervals for the time-averaged values are $0.1T$, which is minimum period
among the superposed sinusoidal functions [Trajectory optimization, $Re = 10,000$, $k = 3.93$, $\alpha = 8°$]
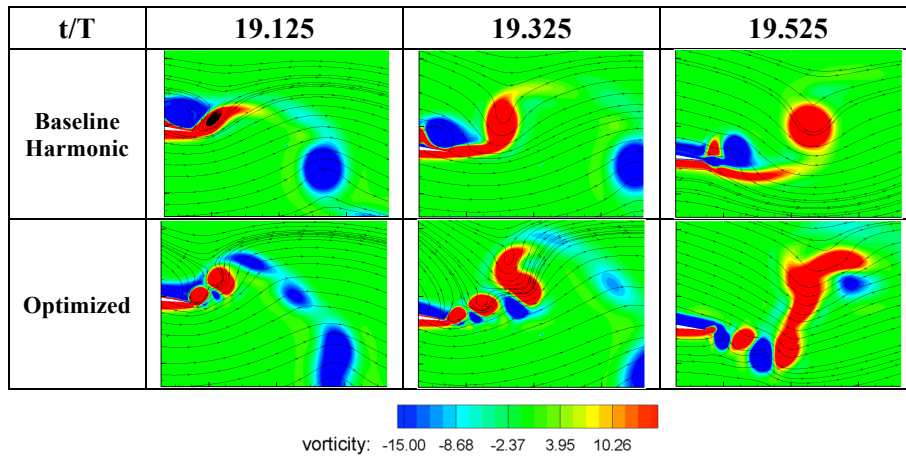

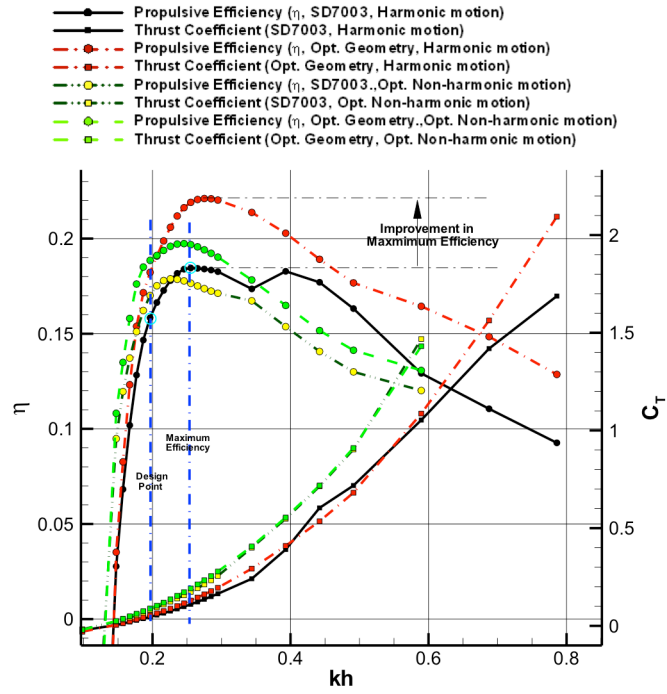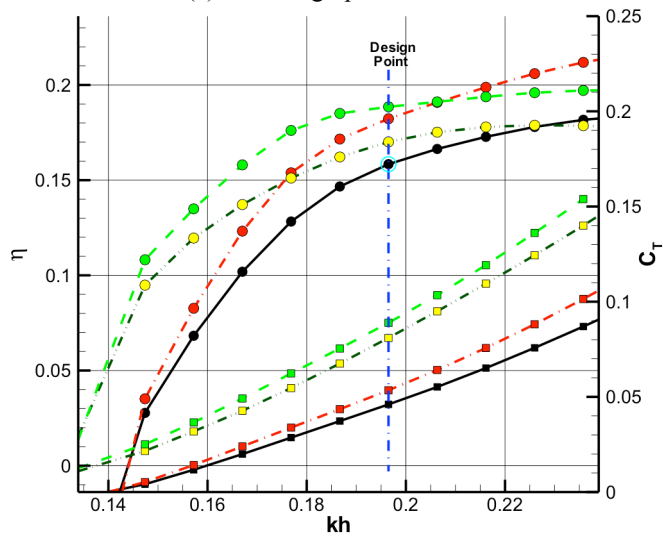vorticity: -15.00 -8.68 -2.37 3.95 10.26

Fig. 27. Comparison of vorticity contours and streamlines between baseline and optimized trajectories at trailing
edge during the positive net thrust generation
[$Re = 10,000$, $k = 3.93$, $h_0 = 0.05$, $\alpha = 8°$, 20th cycle, trajectory optimization, fine grid]

(a) Off-design performance

(b) Off-design performance around the design point

Fig. 28. Comparison of aerodynamic performance at on/off-design conditions, (b) showing the expanded view near the design point [$Re = 10{,}000$, $k = 3.93$, $\alpha = 8°$]